

MASTER THESIS PROJECT AT
KUNGLIGA TEKNISKA HÖGSKOLAN
DEPARTMENT OF MICRO- AND NANOSYSTEMS

Development and characterization of crack-initiated and electromigrated tunnelling nanogap junctions

Author:
Fabrizio Gota

.....

Polytechnic University of Turin supervisors:
Matteo Cocuzza

.....

Francesca Frascella

.....

Kungliga Tekniska Högskolan supervisors:
Frank Niklaus
Valentin Dubois

MASTER'S DEGREE IN NANOTECHNOLOGIES FOR ICTs FROM
POLYTECHNIC UNIVERSITY OF TURIN



From March, 1st to August, 31st 2018

Contents

1	Abstract	2
2	Motivation and background	3
2.1	Nanogap applications	3
2.2	Fabrication of nanogaps	5
3	Introduction to the Thesis project	10
3.1	Crack-defined break-junctions	10
3.2	Samples used	13
3.3	Protocol for electromigration	14
4	Theory	16
4.1	Electromigration	16
4.2	Ballistic regime	18
4.3	Landauer formula	18
4.4	Tunnelling junction and Simmons' model	20
4.5	Reduced work function	21
5	Experimental setup	22
5.1	Mechanical probe station	22
6	Results and discussion	26
6.1	Preliminary tests on 1b	26
6.1.1	Minimum breakdown voltage and typical electromigration . .	26
6.1.2	Investigation of electromigration protocol	29
6.1.3	Conductance below conductance quantum	30
6.1.4	Final considerations on 1b	31
6.2	Large statistical analysis on 1a	32
6.2.1	Resistance distribution	33
6.2.2	Analysis of electromigration: part 1	35
6.2.3	Analysis of electromigration: part 2	36
6.2.4	Two typical electromigration processes	38
6.2.5	Final considerations on 1a	40
6.3	Second Oxygen ICP on 1b	40
6.4	Long Oxygen ICP tests on 1d	42
6.5	SEM influence on 1c	47
6.6	Final results on 1c	51
6.6.1	Statistical analysis of electromigration	51
6.6.2	Typical electromigration processes	55
6.6.3	Final considerations on 1c, die #2	57
7	Conclusions	58
8	Appendices	63

1 Abstract

Nanogap junctions consist of two electrically conducting tips separated by a nanometric gap. To detect tunnelling currents, sub-3 nm gaps are required. They enable a variety of applications, including biomolecular detection [1], molecular electronics [2], nano-photonics [3] and plasmonics [4]. Today different techniques are used to reliably create tunnelling nanogap junctions. These techniques operate locally on one device, using a bulky external apparatus with a feedback mechanism to control the breaking of a single device. For this reason the use of tunnelling nanogap junctions is still confined to research purposes. In this Master Thesis project a new approach to create tunnelling nanogap junctions is developed, through electromigration of gold ligaments formed with the fabrication process of crack-defined break-junctions (CDBJs) [5]. The nanometric dimensions of the gold ligaments, created on wafer-scale through the CDBJs technique, allow adopting a simple electromigration process, which does not require feedback systems. The electromigration procedure consists simply in the application of a fixed voltage difference to two probing pads. Moreover, dealing with suspended ligaments, the common issue of the generation of debris in the vicinity of the gap in electromigrated junctions is avoided. A fabrication yield of tunnelling nanogap junctions equal to 37% is demonstrated.

2 Motivation and background

In the past 50 years, human society has experienced the greatest technological revolution of its history. Its driving force is linked to the exponential performances of semiconductor industry. Moore's law has foreseen the exponential pace of increase of transistor density in a chip [6], which indeed doubled every two years until the present time. However Moore's law is expected to end, due to physical limits of scaling in solid state devices and increasing R&D and fabrication costs. The 2013 International Technology Roadmap for Semiconductors (ITRS) already predicted that fundamental limits of 2D scaling are going to be reached for all devices between 2015 and 2021 [7]. Advancements in transistor density will probably exploit 3D architectures, but new technological solutions, beyond CMOS, are more and more an hot topic. Two new research fields were born in the last years to breathe new life in the semiconductor industry. ITRS has named these fields *More Moore* and *More than Moore*. The first term relates to the development of new technologies which can overcome the limits of conventional 2D CMOS architectures, being able to reach the limits of downsizing and/or providing more computational power thanks to innovative architectures and technologies. Molecular electronics [8] and quantum computing [9] are two examples of research fields falling into this group. *More than Moore* on the other hand refers to the increasing necessity to interface and integrate the digital electronic chips to the analogical world. This category include applications in sensing, security, health care, energy efficiency, communication. This unmatched integration enables new technological possibilities and unlimited applications potential, adding value to electronic devices and to the semiconductor industry, which is reaching its limits in scalability.

Both *More Moore* and *More than Moore* can be addressed with nanogap junctions. Nanogap junctions (or nanogap electrodes or nanogaps) consist of two electrodes, separated by a sub-10nm spacing. A list of applications involving nanogaps and techniques to fabricate them are introduced in the following sections.

2.1 Nanogap applications

A variety of innovative applications are enabled by nanogap electrodes.

Biomolecular detection, in particular DNA sequencing, is potentially a huge market for nanogap electrodes. DNA sequencing has been developed for more than 40 years. This technique allows to decode the whole 3-billions sequence of bases in a human genome. A cheap and fast way to achieve it would enable the medicine of the future, personalized medicine [10]. With this new medicine, doctor's prescription will fit the patient DNA, targeting the disease origin and minimizing the therapy side effects. Several billion of dollars were needed at the beginning of the research to sequence a whole human genome. The firsts sequencers were obtained in the early 1970s. The great break-through technique was the Sanger sequencing [11]. With this method, the DNA under study is fragmented in short strings and amplified. A set of steps is required to read in sequence each base. Once all the bases in every single fragment are read, the fragments have to be reordered through

overlapping sequences. Current generation sequencers still rely on fragmentation and base by base reading, but in a massively parallelized way. Cumbersome and highly complex optical methods are required, allowing a human genome sequencing for around US\$1000 in a couple of days [12]. However large scale applications of DNA sequencing as routine test in health care require large improvements in cost and time. Nanopore sequencing is the most serious candidate to reach this ambitious goal. The whole chain of DNA is translocated through a nanopore having a width comparable to that of a DNA base. Several detection techniques can be used to discriminate which base has passed through the pore. Solid state nanogap electrodes, aligned with the pore, have been proved to be able to measure a different level of tunnelling current for each of the 4 DNA bases [1]. Ionic currents solutions instead are already on the market. DNA bases physically impedes the flow of ions through a biological [13] or solid state [14] nanopore. Each base can be then discriminated through the level of the ionic current. These techniques do not require in principle to divide and multiply the DNA. The strand of DNA is translocated one time, with no interruptions, allowing low cost devices and greatly enhanced time efficiency.

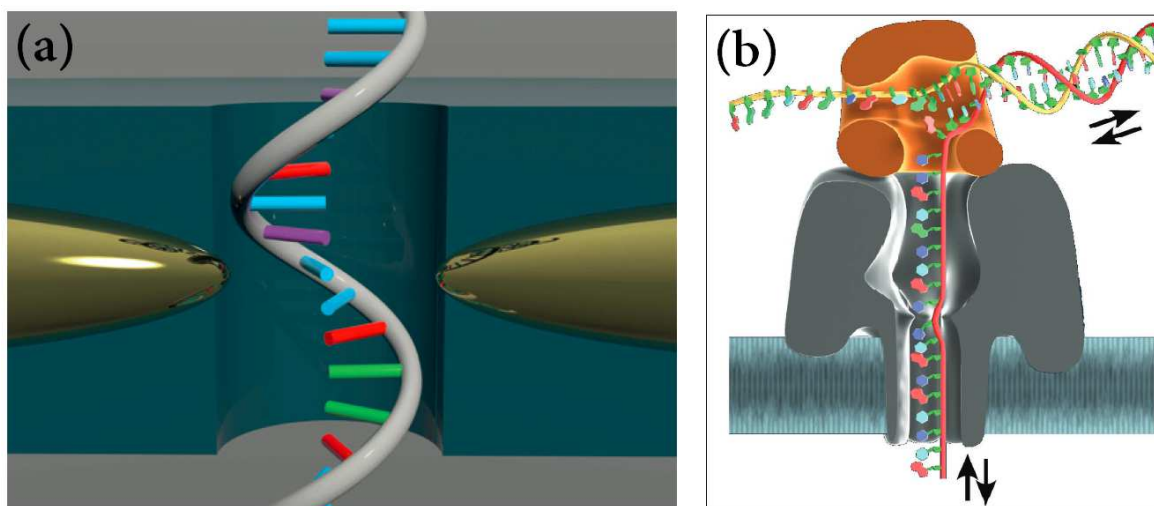


Figure 1: (a) In direct tunnelling sequencing, single-strand DNA is translocated through a nanopore between two metal electrodes that measure a base-mediated tunnelling current. Reproduced by [1]. (b) A biological nanopore is used to allow one strand of DNA through a membrane. The ionic current is modulated by the presence of each DNA base. Reproduced by [13].

In molecular electronics, nanogap electrodes are used to bridge molecules, that would substitute transistors in electronics circuits [15]. Molecules are the ultimate limits to create building blocks in electronic circuits with atomic accuracy, being the smallest stable structure conceivable. In addition, molecules can be produced cheaply in a massively parallelized way, using a chemical reaction in a solution. However a scaffold of nanostructures, which create a stable mechanical and electrical contact, is required to be able to integrate molecules in an electronic chip. Nanogap electrodes are an optimal candidate for this role, besides being already

used to study transport phenomena in molecules. The study and manipulation of transport mechanism in molecules enable a wealth of applications, as for example electrical bio-sensing of binding events [16] and UV light photodetectors [3]. The narrow spacing in nanogap electrodes allows reaching very high electric fields with a relatively low voltage applied. Photonic interactions at the electrode surface enable the coupling of incident photons to the free-electron plasma. Possible applications range from surface enhanced Raman spectroscopy (SERS) [17], nano-antennas [18] and optical rectification [4].

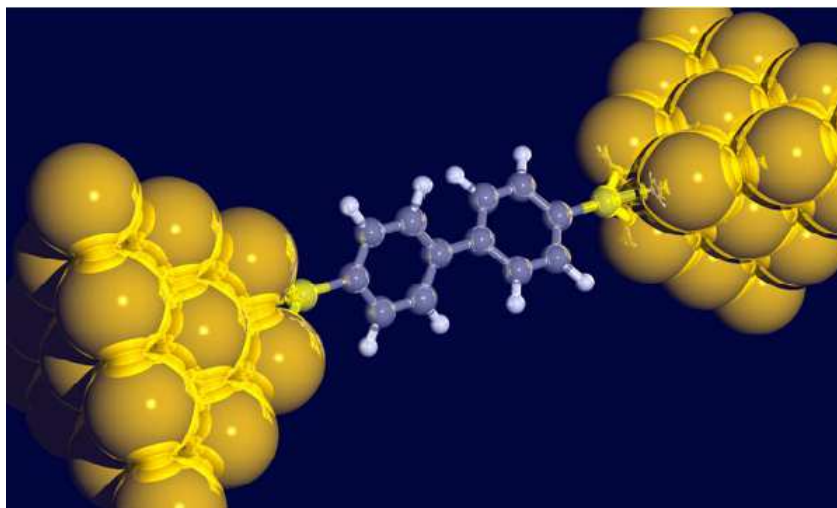


Figure 2: In molecular electronics, a single molecule bridges two electrodes, usually made of gold. Conductance can be modulated with the gate voltage. Reproduced by [19].

Finally, several techniques exploiting nanogaps, able to overcome the practical limits of CMOS technology, are under development. In ultra-fast vacuum transistors, the targeted problem is the limited mobility of electrons in solid-state semiconductors. With this approach, the ultra-high speed is achieved through a vacuum channel, where electrons field emission is controlled by the gate voltage [20]. Ultra-low power nano-electromechanical switches [21] allow quasi-zero leakage in the non-conductive state and operation in harsh environments, through an electrically actuated mechanical switching.

2.2 Fabrication of nanogaps

Nanogap electrodes are currently used in research activities for a variety of applications, including molecular transport investigation [22] and biomolecular detection [23] among others. Two main techniques are used to fabricate nanogaps with detectable tunnelling current (sub-3nm) with a good accuracy and process controllability: feedback-assisted electromigration [24] and mechanically-controlled break-junction (MCBJ) [25].

The former one consist in applying a feedback-adjusted current to a metal nanowire, typically patterned by electron beam lithography (EBL). If the current density is

high enough, the metal ions are moved by the momentum imparted by the electrons. The current density is higher where the cross-section of the wire is smaller. Thus the atoms move away from a constriction, that becomes progressively narrower, and finally when the last atom that bridges the two end of the wire is moved, a nanogap is formed. Since the maximum current density along the wire depends on the minimum cross-section of the wire, which changes over time, a real-time feedback control of the current is needed to avoid catastrophic effects at the end of electromigration, which can cause the uncontrolled creation of a large gap. Joule heating and relaxation effects are the reasons of the poor controllability of the gap size. Feedback control of the process requires ultra-sensitive electrical circuits that make a parallelized fabrication of nanogaps through feedback-controlled electromigration impractical. However this technique is used in research studies, allowing reliable creation of nanogaps, often thanks to self-breaking. Self-breaking occurs when the wire is actively brought to a cross-section consisting of few atoms. Reorganization of the atoms when cooling after the active process and the poor stability of the nanowire promote spontaneous breaking and formation of the gap, avoiding local high temperature at the moment of breakdown [26].

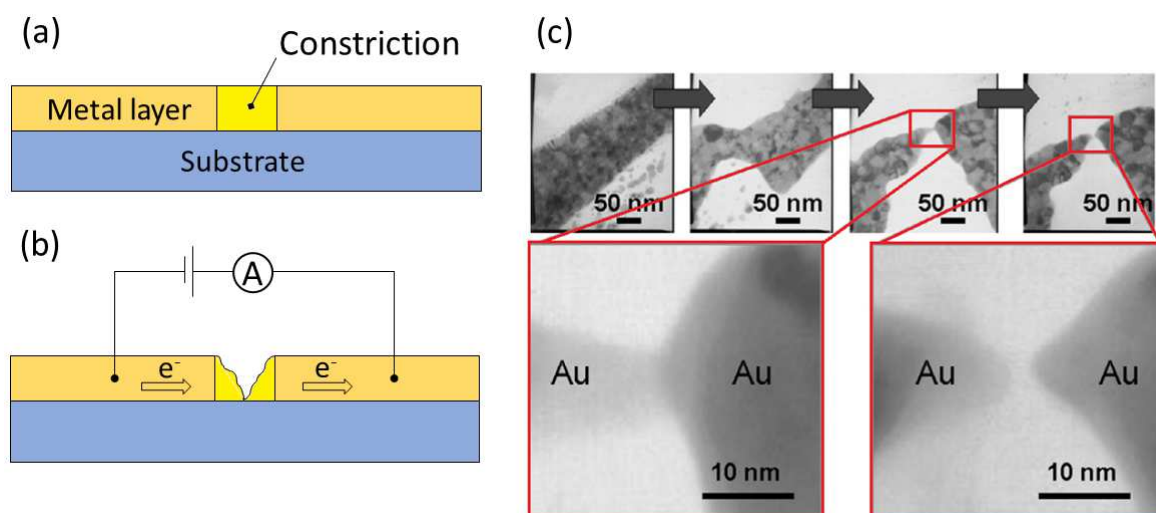


Figure 3: Illustration of the formation of nanogaps through electromigration. (a) A constriction is patterned on a conductive layer. (b) A large current is forced through the constriction, inducing electromigration. (c) SEM images at different stages of nanogap formation (Adapted from [27]).

Mechanically-controlled break-junctions (MCBJs) are created through the use of a three-point wafer-bending stage, which usually utilizes piezoelectric actuators. Bending the wafer, a tensile stress is induced on a suspended metal wire. Since the wire is usually made of a metallic material, it is ductile and breaks after elongation and necking of the constriction. This approach allows to actively control the gap width and reform the conducting wire, operating on the piezoelectric actuators. However only one device at a time can be targeted with this approach.

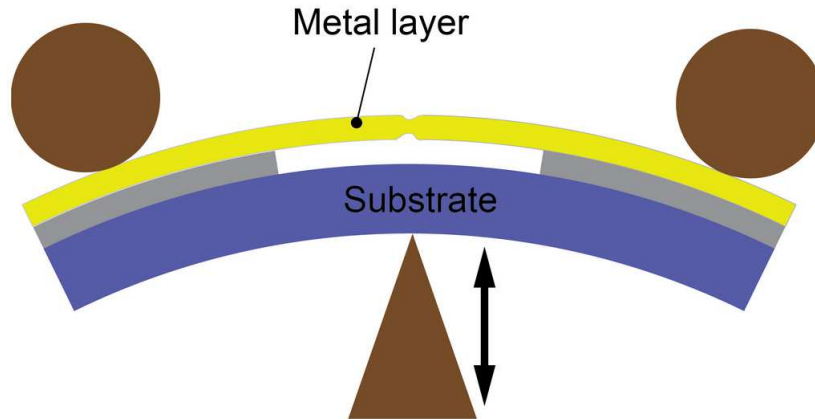


Figure 4: In a mechanically-controlled break-junctions (MCBJ), a three-point wafer-bending stage induces a tensile stress on the metal layer. The gap width in the metal layer can be regulated by actuating the piezoelectric pushing tip.

The two methods just discussed are used to reliably form nanogap electrodes, but require a complicated apparatus with feedback control and therefore do not enable the parallelization of the technique to multiple devices. A number of techniques can be used for the wafer-scale fabrication of nanogaps, and can be divided in three categories: subtractive, additive and splitting techniques. In the subtractive category, the electrode material is deposited and then selectively removed to create the nanogap. Selective deposition is used instead in the additive fabrication of nanogaps. Finally, with splitting techniques, material is neither removed nor added.

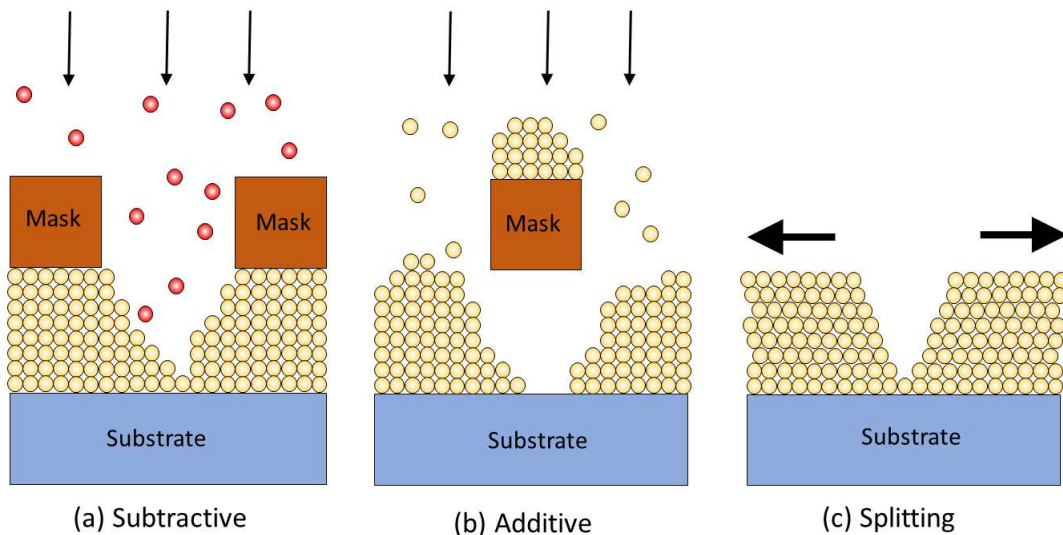


Figure 5: Schematic illustrations of the three nanogap manufacturing techniques: (a) subtractive, where electrode material is removed from the nanogap, (b) additive, where the nanogap is formed by selective deposition of the electrode material, and (c) splitting, where the nanogap is formed without adding or removing material.

In the **subtractive** group, optical lithography is certainly the most widespread tech-

nique in nanofabrication. However, optical lithography is limited by the wavelength of the light used to impress the resist. The 7nm logic node fabricated using extreme ultraviolet light is currently under development for mass-production [28]. However, the tools needed to produce these nanometric features are ultra-expensive and currently are affordable only for mass-production of electronic chips. Moreover, 7nm is still far from the required sub-3nm gap that allows tunnelling current and enables important applications of nanogap electrodes, e.g. DNA sequencing. Electron beam lithography (EBL) have been proved to produce sub-10nm features, with potential for sub-5nm, even if edge roughness increases a lot in this range [29]. The main drawback of this technique is the low throughput, which is limited by the nature of EBL, which is a serial process.

Scanning probe lithography (SPL) is another subtractive technique in which an atomically sharp tip is scanned in contact or in close proximity to the substrate surface, in a similar fashion of scanning tunnelling microscope (STM) and atomic force microscope (AFM). A pattern is created in the masking layer by thermal, mechanical, or electrical field manipulation in the vicinity of the tip location [30]. The minimum gap width that SPL is able to create depends on the radius of the probe tip, which is usually in the range of ~ 3 nm. SPL is a serial technique, however an array of tips can be arranged to speed up the process.

Generally, lithography meets a sub-10nm limitation that will probably remain a major obstacle in the future. Fabrication of nanogap electrodes is made difficult by the limited reliability in the etching of noble metals, which are required in most of the applications. Reliability and surface roughness introduced by the etching step are the main limitations.

Focused ion beam (FIB) direct etching is another subtractive technique, which does not require any lithographic step. Thus the quality of the nanometric features depends only on one step, which is the direct etching. However, the sputtering process creates inevitably atomic scale roughness and ion implantation can be detrimental to the electronic and photonic properties of the target layer [31]. Most importantly, FIB is a serial process, which moreover often requires in-situ monitoring to control the size of the gap.

In **additive** techniques, the electrode material is deposited over the substrate. The gap is created due to the presence of a shadow mask [32] or due to narrowing of a larger gap after the metal deposition [33]. In the first case the quality of the facing electrode surfaces created by shadow mask deposition is governed by the line edge roughness of the shadow mask, as well as the growth behavior of the deposited electrode material on the surface of the substrate [34]. For the second process, to obtain reproducible nanogap electrodes after the gap narrowing, extremely accurate patterning of the initial electrode pairs is critically important. These requirements severely limit the expected improvement in scalability of these manufacturing methods. To produce sub-3nm features in-situ monitoring during the deposition is needed.

The **splitting** techniques rely on breaking of a wire thanks to a pulling action, inducing the formation of a gap. MCBJ are an example of technique in this group. The wire material is usually a ductile metal, which can form sharp tips as already

discussed in this section.

Gaps can also be formed in brittle materials, for example with the crack-junctions (CJ) methodology. In this approach, a wire is deposited and patterned above a sacrificial layer. The wire material has a larger coefficient of thermal expansion and is deposited at a high temperature, generating a tensile stress over the whole length of the wire when the sample is cooled down to room temperature. Notches are patterned on the wire, creating a region where the cross-sectional area is considerably smaller. When the sacrificial layer is etched away, the wire is free-standing. The stress redistributes and concentrates in the notched area. If the stress overcome the fracture strength, a gap is created. The gap final size is not connected to a lithographic process, but to the retraction of the two electrodes when the gap is formed, which is directly proportional to the length of the wire released region [35]. Since the fabrication is based on standard optical lithography and etching, it is a wafer-scale process. Brittle splitting on CJs has been demonstrated with a manufacturing yield of devices with sub-3nm gaps of 40% [35], [36].

The crack in a brittle material generates two electrodes with parallel surfaces. However most of the applications of nanogap electrodes require a noble metal, usually gold, to be able to generate tunnelling currents and to have a good mechanical and electrical contact with molecules. Metals are ductile and thus require a different technique to create a nanogap electrode. To achieve this goal, the so-called crack-defined break-junctions (CDBJs) have been developed [5]. These devices, being the starting platform on which this thesis work is developed, are introduced in the next chapter.

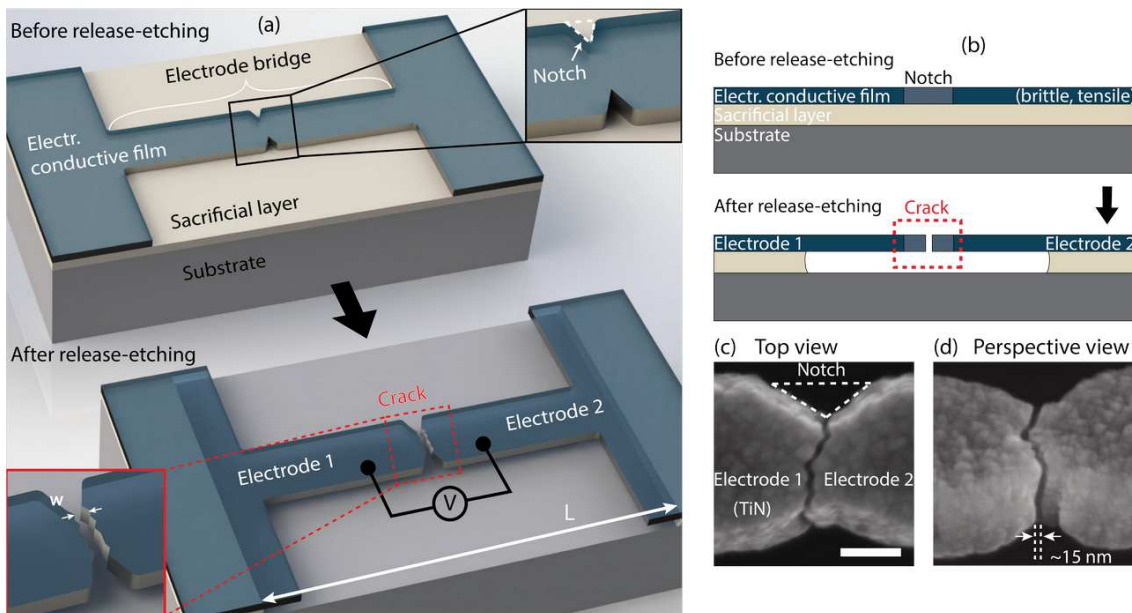


Figure 6: (a) and (b) illustrate the perspective and cross-sectional views of the CJs fabrication method. (c) and (d) show top and perspective view SEM images of a 10 nm wide crack-defined nanogap between titanium nitride (TiN) electrodes. Adapted from [35].

3 Introduction to the Thesis project

3.1 Crack-defined break-junctions

In this Thesis project, an investigation of a simple, feedback-free electromigration process on ligaments formed in the process leading to the so-called crack-defined break-junctions (abbreviated CDBJ), is performed. A CDBJ exploits the controlled generation of a crack in a brittle titanium nitride (TiN) layer to generate a nanogap in a conductive ductile layer, deposited on top of the brittle material. When the crack in TiN is generated, a pulling action is generated on the gold layer in correspondence of the crack-line. Being a ductile material, the gold layer elongates. If the pulling action is large enough, voids are generated in the gold material, highlighting ligaments that connect the two sides of the gold bridge. A further increase of the pulling displacement can break the ligaments and generate in this way a nanogap separated by two sharp metallic tips [5]. This last stage correspond to a CDBJ. In this work however Type-2 junctions (see Fig.7) are investigated, where the devices have at least one ligament bridging the two electrodes.

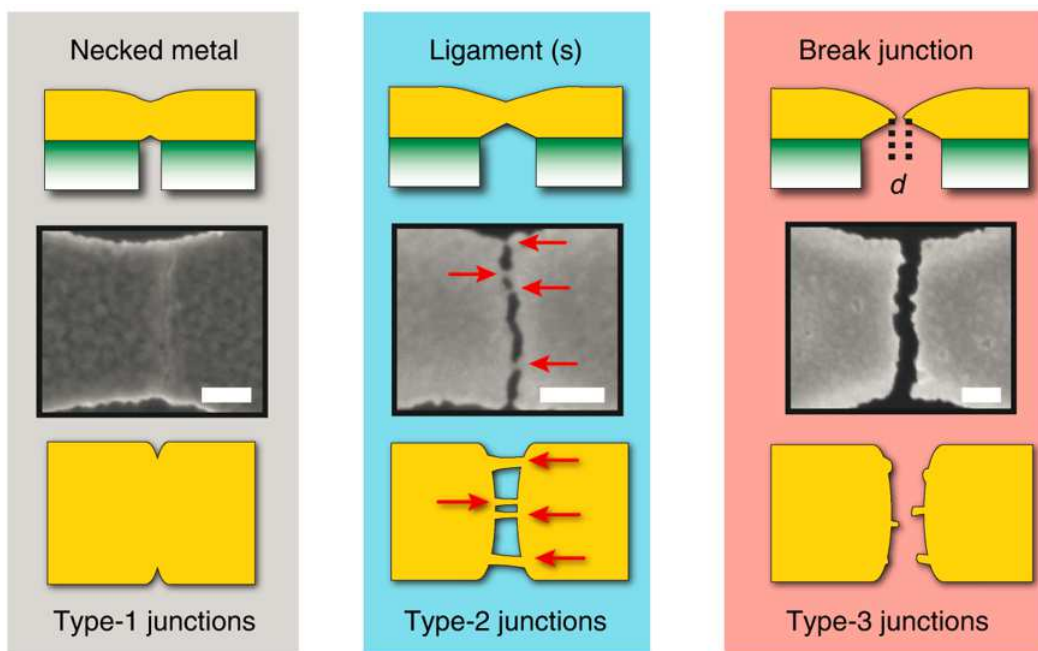


Figure 7: Outcomes of different pulling forces on the gold layer. For small pulling actions, necking of the gold layer is observed. Increasing the brittle material crack width, one or more ligaments are outlined. This is the starting stage for this thesis work. At larger pulling forces, the ligaments break and form a nanogap. The number of ligaments created during this process depends on the constriction width. Reproduced from [5].

In this project, the samples are processed with the following fabrication steps. A 200 nm thermal oxide is grown for passivation over a 525 μm -thick 4-inches silicon wafer. Over the silicon oxide is deposited the sacrificial layer, which consist of a 200 nm-thick amorphous silicon (a-Si), with a plasma-enhanced CVD process. On top of a-Si, a 50 nm-thick titanium nitride (TiN) film is deposited with atomic layer

deposition (ALD). This layer is the brittle material, in which the crack-formation will take place. ALD deposition of TiN takes place at 350 °C. Due to the larger coefficient of thermal expansion (CTE) of TiN compared to that of a-Si, a tensile stress builds up in the TiN layer when the wafer cools down to room temperature. Then the electrode material is deposited over TiN, which consist of a 10 nm-thick gold (Au) layer, with a 3 nm-thick chromium (Cr) layer to improve adhesion to the TiN. Gold is used for its chemical stability, high electrical conductivity and ability to form covalent bonds with functional groups in molecules. The last feature is essential for molecular electronics applications. Moreover it is one the most studied and understood material in micro- and nanofabrication, being used in a large amount of applications. Finally it meets the requirement of being ductile down to the atomic level, allowing the fabrication of atomically sharp tips after mechanical elongation. Once the deposition of the layers is completed, a notched bridge structure is patterned on the TiN-Cr-Au stack with conventional lithography and etching. First a resist layer is spin-coated on the wafer. A wafer-scale stepper lithography is used to outline the notched bridges in the resist. The resist mask is used to selectively etch first the thin Cr and Au layers with ion beam etching and then TiN through plasma etching. It has to be remarked that up to this point the structure does not present any crack and the TiN-Cr-Au stack lies on a-Si. The internal tensile stress of the stack is distributed over the whole length of the bridge. When the a-Si is selectively removed by a dry plasma etch, the bridge is free-standing. Since the TiN layer is no more constrained to a-Si, the internal tensile stress redistributes and concentrates in the notched area, where the cross-section is minimum. The higher the area of the bridge released, the higher the built up stress in the notched area, that at a certain moment overcome the fracture strength of TiN. At this point a crack is formed across the notches of the TiN layer. Being a brittle material, the crack forms abruptly and follows the grain boundaries of TiN. The tensile stress, originating from the large CTE mismatch between TiN and Si, is released by retraction of the two TiN cantilevers that once constituted the bridge. It has been demonstrated that the retraction, and so the gap width w in TiN, is directly proportional to the length of the bridge L , released during the plasma etch of a-Si [35]:

$$d = \epsilon \cdot L \quad (1)$$

The proportionality constant ϵ is the elastic strain of TiN, which in experimental studies was found to be $\epsilon = 2.7 \text{ nm}/\mu\text{m}$ [5]. Controlling nanometer sized features designing micrometric long bridges allows to create in a parallel fashion millions of gaps within the tunnelling range of 3 nm. However the cracks have to be formed in a brittle material, which usually is not highly conductive. Moreover the crack generates parallel surfaces, while sharp tips are best suited for many applications of nanogap junctions, e.g. DNA sequencing. Gold is deposited over TiN to tackle these issues. When the fracture in titanium nitride is generated, the gold layer above the crack-line experience in turn a tensile stress due to retraction of TiN. A crack is not formed in Au, being a ductile material. Instead it elongates and necks. Generally voids are formed within the neck for high pulling forces, outlining multiple ligaments, that break one by one at larger displacement of TiN. If the pulling force, directly proportional to the gap width d , is large enough, the last standing ligament

breaks and forms a nanometric gap. The last stage is the outcome of a CDBJ, while for this thesis work were used the devices showing at least one ligament connecting the two electrodes.

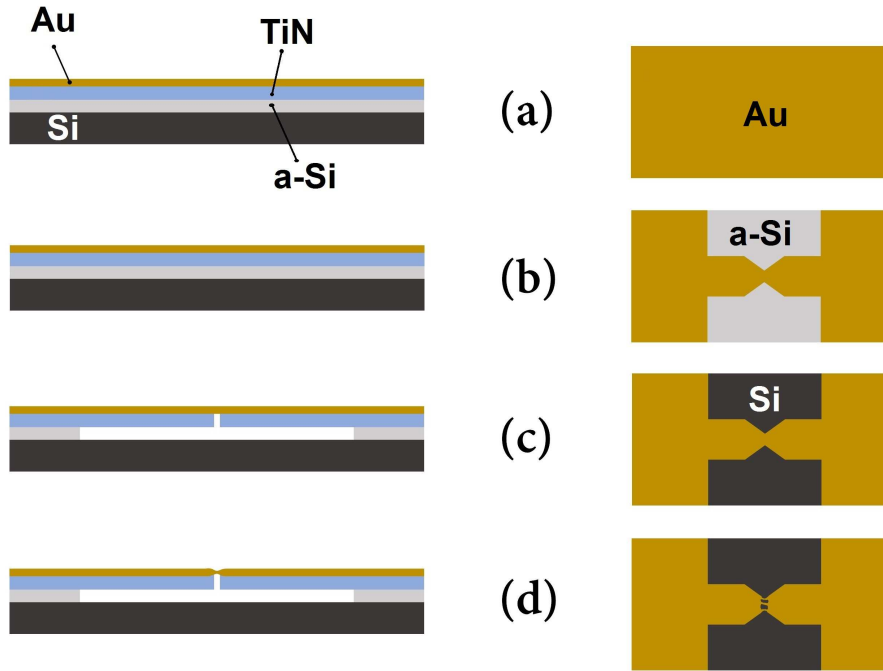


Figure 8: Out of scale illustration of the fabrication of the devices that underwent electromigration in this work. (a) Deposition of the layers (Cr is not illustrated here). (b) Definition of the bridge through selective etching of the Au-Cr-TiN stack. (c) Selective etching of a-Si. The crack is formed across the TiN constriction. (d) The pulling action due to TiN retraction necks and strains the gold layer, creating ligaments in correspondence of the crack line.

A wafer scale fabrication of CDBJs was demonstrated, allowing a density up to 7 millions junctions per cm^2 [5]. Crack formation in the TiN layer was observed in the 99.7% of the devices, proving reliable and feasible for large scale manufacturing. However the success rate of obtaining a gap also in the gold layer is considerably lower. 7% of the devices within the electrically probed junctions, showed a measurable tunnelling current, which relates to a gap smaller than 3 nm. The remaining ones showed an ohmic behavior (40%), revealing the presence of ligaments, or formed gaps too large ($R > 100 \text{ T}\Omega$) to allow detecting a tunnelling current (52%). In this work, the devices presenting ligaments were analyzed to investigate a simple, feedback-free electromigration process. The yield of useful tunnelling junctions after the electromigration process is compared to that of CDBJs. Strengths and weaknesses of this method are analyzed and possible improvements and applications are discussed.

3.2 Samples used

A 4-inch wafer was available for the thesis project. The wafer was cleaved in four parts and, after the fabrication steps described in the previous section, each one underwent a different post-processing, as it will be described. The four parts were called 1a, 1b, 1c and 1d as shown in Fig.9. A big portion of the quarter 1b was devoted to another research project.

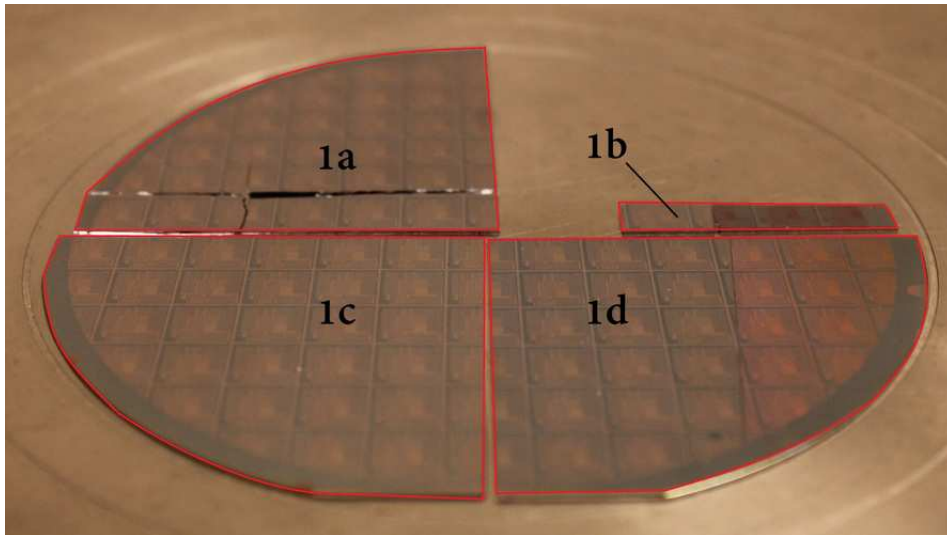


Figure 9: Wafer used in this project, with the names of the 4 samples.

Within each die, several designs were present, including other test structures used for the characterization of the CJs and CDBJs. In this study for each die two columns, containing each 30 junctions were investigated (see Appendix 1, Fig.34). The two columns differ in the design. In particular the first column, named Simple 2 (S2), shows a wider neck (~ 250 nm) than the second one (~ 100 nm), called Simple 3 (S3). Having a wider neck, the junctions present in the column S2 present often more than one ligament, up to 4-5. The other difference between the two designs lies in the different angle of the notches, with S2 showing a wider angle (100°) than S3 (80°). The two electrodes are probed through two $100\ \mu\text{m} \times 100\ \mu\text{m}$ pads.

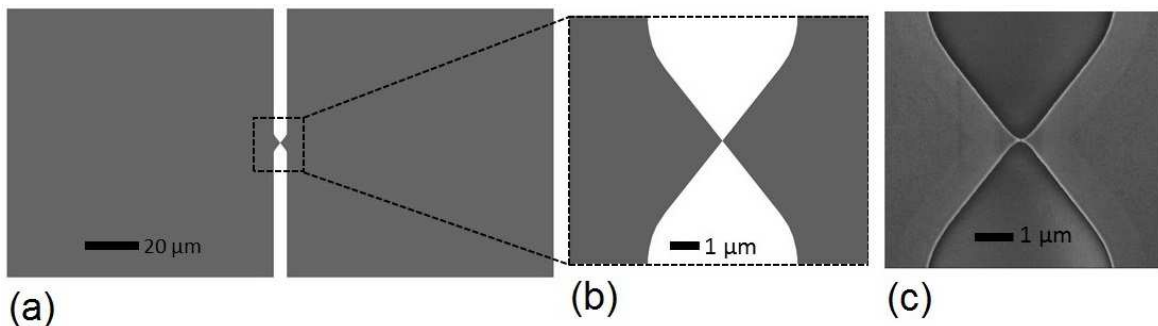


Figure 10: Illustration of the S3 design. (a) Mask design of the two electrodes connected to the probing pads. (b) Focus on the design of the notches. (c) SEM image of a device with S3 design.

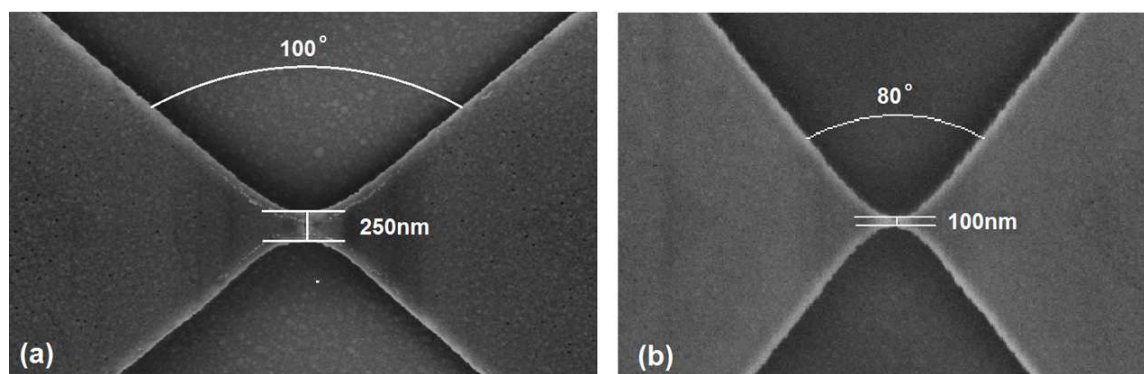


Figure 11: SEM pictures of the two designs used in this work, with the width of the constriction and the angle of the notches: (a) S2 and (b) S3.

3.3 Protocol for electromigration

The aim of this work is to develop an optimal method to generate tunnelling nanogap junctions in the gold layer, starting from the devices that showed an ohmic behavior, that is to say the ones with one or more ligaments connecting the two Au electrodes. Electromigration is adopted to move away Au atoms from the ligaments and create a nanogap in correspondence of the TiN crack-line.

As already mentioned in Chapter 2, feedback-assisted electromigration on nanowires is already used in the research environment for the fabrication of nanometer sized gaps. However, the fabrication of a nanowire, which width is in the sub-100nm range, requires patterning with electron beam lithography (EBL). This technique allows reaching a sub-10nm, but prevents the parallel fabrication of the bridges, being a serial technique. Moreover, the feedback system used to perform electromigration allows creating a gap only for one device at a time. For these reasons, electromigrated nanogaps have been used only for research purposes, having a very limited throughput of useful devices. Another common drawback of electromigrated nanogaps is the formation of the electrode material debris during electromigration in the vicinity of the nanogap. These gold island may mislead molecular electronics results, giving signatures of Coulomb blockade and Kondo effects, similar to the ones observable in conduction through a single molecule [37],[38], and in general promoting a conduction mechanism which is not the direct tunnelling between the two electrodes. Self-breaking, in which the instability of a wire with a constriction actively narrowed to a few atoms in the cross-section is exploited to generate a gap [26], and suspended electrodes can be used to alleviate this problem.

In this work a very simple methodology, consisting in applying a constant voltage to the two pads connected to the two sides of the bridge is adopted. The nanometric cross-section of the ligaments allows observing electromigration for limited voltages, down to 150 mV. The low voltage required prevents melting and catastrophic gap formation during electromigration. This simple technique does not require any feedback control, which usually is performed through complex and cumbersome external apparatuses. Only a voltage source is needed for the technique presented in this

work. In addition, being the gold layer suspended in correspondence of the crack-line, gold debris resulting from electromigration cannot be localized in the middle of the gap. As a consequence, they are not detrimental.

The procedure, which do not require any feedback system, and consist simply in applying a fixed voltage, could be performed in parallel to several devices and represent a first step in the realization of a large-scale production of sharp-tipped gold nanogap electrodes. The parallelization of the procedure has not been tested during the thesis project, but it represents a promising future research direction.

4 Theory

4.1 Electromigration

Electromigration is widely known in the scientific community, being one of the main reasons for failure in early electronic chips [39]. Electromigration occurs when a large current density flows through a metallic material. It consists in the movement of the metal ions due to the momentum transferred by the electrons. A combination of several parameters has to be satisfied to start the ion migration. Even if generally the beginning of electromigration is attributed to the overcoming of a critical current density for a specific material, the process depends also on other parameters, for example the local temperature of the metal [40] and the temperature gradient along the wire [41]. Providing a full description of this phenomenon is a formidable task. The theory of irreversible processes however gives a good insight on the origin of electromigration. In this context, all the fluxes and forces operating are considered. Three fluxes are present, namely the electrons flux J_e , the metal ions flux J_m , and the energy flux J_u . The fluxes are caused by 3 forces (or equivalently 3 potential gradients X). The first two are related to the electrons and ions potential gradients $X_j = -\nabla\mu_{ec}^j$, where $j = \{e, m\}$ and identifies electrons and metal ions respectively. $\mu_{ec} = \mu + Ze\phi$ is the electrochemical potential, with ϕ being the electrostatic potential, μ the chemical potential and Z the particle charge (positive for metal ions, -1 for electrons). The third force is related to local temperature gradient: $X_u = \nabla(1/T)$. The theory of irreversible processes leads to a set of 3 coupled equations [40]:

$$J_e = -L_{e,m} \cdot \nabla\left(\frac{\mu_{ec}^m}{T}\right) - L_{e,e} \cdot \nabla\left(\frac{\mu_{ec}^e}{T}\right) - L_{e,u} \cdot \left(\frac{\nabla T}{T^2}\right) \quad (2)$$

$$J_m = -L_{m,m} \cdot \nabla\left(\frac{\mu_{ec}^m}{T}\right) - L_{m,e} \cdot \nabla\left(\frac{\mu_{ec}^e}{T}\right) - L_{m,u} \cdot \left(\frac{\nabla T}{T^2}\right) \quad (3)$$

$$J_u = -L_{u,m} \cdot \nabla\left(\frac{\mu_{ec}^m}{T}\right) - L_{u,e} \cdot \nabla\left(\frac{\mu_{ec}^e}{T}\right) - L_{u,u} \cdot \left(\frac{\nabla T}{T^2}\right) \quad (4)$$

$L_{i,j}$ are phenomenological constants that follow the Onsager relations $L_{i,j} = L_{j,i}$. The flux of metal ions J_m depends on several factors, including local temperature and temperature gradients. Indeed this theory includes besides electromigration, also thermodiffusion and thermoelectric effect. This equation can be simplified with some reasonable assumptions for metals. First, $\nabla\mu^e$ can be neglected for materials with a high conductivity. Thermodiffusion effects can also be ignored, as proved for gold electrodes [40]. Moreover in a metal the flux of charges is basically only related to electrons. As a consequence $-\nabla\phi = \rho j$, where ρ is the electrical resistivity. Finally the equation of the flux of metal ions is expressed at:

$$J_m = -L_{m,m} \cdot \left(\frac{\nabla\mu^m - Z^*e\rho j}{T}\right), \quad (5)$$

where it has been introduced an effective charge of the ions, defined as $Z^* = Z - L_{m,e}/L_{m,m}$. The corrective term $L_{m,e}/L_{m,m}$ is due to momentum transfer from the electrons to the ions. Considering that during electromigration generally $L_{m,e}/L_{m,m} \gg Z$ [42], the effective charge Z^* is negative. Thus the net force acting on the ions is in the direction of the flux of electrons.

Further modifications can be performed, substituting $\nabla\mu^m = \Omega \cdot d\sigma/dx$, which is the force due to stress σ . Eq.5 is rewritten as

$$J_m = -L_{m,m} \cdot \left(\frac{\Omega \cdot \Delta\sigma/L - Z^* e \rho j}{T} \right), \quad (6)$$

with $\Delta\sigma$ the total stress over the length L of the wire. As long as $\Delta\sigma < \Delta\sigma_{max}$, the stress gradient compensates the electromigration force and the total ions flux J_m is null. The onset of ions migration is observed when the electron current density reach the critical current density $J_{min} = \Omega \cdot \Delta\sigma_{max}/Z^* e \rho L$.

To develop further the model, the diffusion constant D is introduced. According to the Einstein relation it can be expressed as: $D = L_{m,m}^* \cdot d\mu/dc$, with c the concentration of metal ions and the chemical potential $\mu = kT \cdot \ln c$. The diffusion constant can also be expressed as $D = D_0 \cdot \exp(-E_a/kT)$, where E_a is the activation energy of diffusion on the surface, which for gold is 0.12eV [40]. Combining these two relations, the phenomenological constant can be written as $L_{m,m}^* = (D_0 c/kT) \exp(-E_a/kT)$. Finally, the metal atoms flux J_m during the electromigration process can be approximated as:

$$\begin{aligned} J_m &\simeq 0 && , j < j_{min} \\ J_m &= \frac{\alpha}{T} \cdot (j - j_{min}) \cdot e^{-E_a/kT} && , j \geq j_{min} \end{aligned} \quad (7)$$

Here $\alpha = cD_0Z^*e\rho/k < 0$ ($Z^* < 0$ in electromigration conditions). The negative value of α implies that when electromigration start, the ion and electron current density have opposite sign, that is to say that ions move in the same direction of electrons flow.

For gold electrodes $j_{min} \simeq 3 \cdot 10^8 A/cm^2$ at room temperature. This critical electron current density depends on the environment temperature T_{env} . Trouwborst et al. [40] computed that an increase of $\sim 50\%$ is needed when decreasing the temperature from 295K to 4.2K. This is related to the fact that electromigration starts when the wire increases its local temperature to a critical value T_c due to Joule heating, which experimentally resulted in $\sim 400K$ for $T_{env} = 4.2K, 77K$ and $295K$. At lower T_{env} , a larger current density is needed to reach the critical local temperature. The weak dependence of the critical temperature from the environment temperature is related to the need to activate the metal ions mobility, which requires a specific local temperature. The great relevance of the wire local temperature is also evident in Eq.7, with the metal ions current density depending exponentially on it. The exponential term derives from the diffusion formula of the ions on the surface.

It has to be remarked that electromigration involve only the ions on the surface of the wire. Real-time TEM imaging performed during different stages of the electromigration process demonstrates it [43].

As discussed above, Joule heating is required for the onset of the electromigration

process. However, an excessive heating can bring about catastrophic consequences for the nanogap, particularly in the last stages before the gap formation. In these moments, the cross-section of the wire is minimum and the current density maximum. High temperatures reached at this stage can lead to melting and structural reorganization.

4.2 Ballistic regime

When the length of the constriction reaches nanometric values, electrons can enter in the ballistic transport regime. In this regime, electrons do not experience scattering collisions during their transition through the constriction. Collisions involve the interaction with defects, impurities, phonons and other electrons, and are responsible for the electrical resistance of a macroscopic metal. Ballistic regime is valid when the length of the conduction channel respects the following relation:

$$\lambda_F < L < L_m \quad (8)$$

where λ_F is the Fermi wavelength and L_m is the electrons mean free path in the metal. The Fermi wavelength is linked to the Fermi energy level by the following relations:

$$\lambda_F = \frac{2\pi}{k_F}, \quad E_F = \frac{\hbar^2 k_F^2}{2m} \quad (9)$$

For gold $\lambda_F \simeq 0.5\text{nm}$ and $L_m \simeq 14\text{nm}$ [44]. When the nanowire is shorter than the Fermi wavelength, interference phenomena play a role in the transport dynamics of the electrons. On the other side, when $L > L_m$, electrons undergo non-negligible scattering events and the electrical resistance follows the laws of macroscopic metals. Gold ligaments created in CDBJ satisfy the criteria to enter in the ballistic regime and the effects visible before breakdown are clearly related to ballistic transport. In particular quantized conductance steps are observed and can be explained with the Landauer formula.

4.3 Landauer formula

As reported in the previous section, when the constriction length is just few nanometers, the system enters the ballistic transport regime. Electrons flow through the nanowire without scattering. However a finite resistance is still measurable and is due to thermalization of electrons reaching a reservoir with a lower energy than their kinetic energy.

In a 1D wire, with unitary transmission probability (so an ideal ballistic system),

connecting two reservoirs of potential μ_1 and μ_2 :

$$\begin{aligned}
 I &= e \cdot \int_0^\infty v(k) \cdot n(k) \cdot f_1(k) dk - e \cdot \int_0^\infty v(k') \cdot n(k') \cdot f_2(k') dk' \\
 &= e \cdot \int_0^{\mu_1} \frac{\hbar k}{m} \cdot \frac{1}{\pi} \cdot \frac{dk}{dE} dE - e \cdot \int_0^{\mu_2} \frac{\hbar k}{m} \cdot \frac{1}{\pi} \cdot \frac{dk'}{dE'} dE' \\
 &= e \cdot \int_{\mu_2}^{\mu_1} \frac{\hbar k}{m} \cdot \frac{1}{\pi} \cdot \frac{dk}{dE} dE = \frac{2e}{h} \cdot (\mu_1 - \mu_2) = \frac{2e^2}{h} \cdot V
 \end{aligned} \tag{10}$$

$$G_0 = \frac{I}{V} = \frac{2e^2}{h} \simeq 77 \mu\text{S} \tag{11}$$

$$R_0 = \frac{h}{2e^2} \simeq 12.9 \text{ k}\Omega \tag{12}$$

In Eq.10 $v(k)$ is the electron velocity and $n(k)$ the density of states. Eq.11 is valid for a 1D system, with 1 channel and transmission probability $T=1$. To generalize the equation to systems with more than one conducting channel and with non ideal transmission probability, Eq.11 has to be multiplied by the number of conducting channels M and the transmission probability T .

$$G = \frac{I}{V} = \frac{2e^2}{h} \cdot M \cdot T \tag{13}$$

The number of channels are related to the number of energy sub-bands, which are a result of the confinement of the electronic states perpendicularly to the direction of the electrons flow. The total current is the sum of the currents given by each sub-band. The number of modes is easily computed from the basic quantum mechanical problem of the infinite quantum well. The electronic states have quantized energy levels. For simplicity's sake, it is assumed that the cross section of the wire is a square with side length W . Quantum mechanic theory gives:

$$E_{n_x, n_y} = \frac{\hbar^2 \cdot k_{n_x, n_y}^2}{2m} \tag{14}$$

Here $k_{n_x, n_y} = \left| \frac{\pi}{W} \cdot (n_x \hat{x} + n_y \hat{y}) \right|$. The levels are occupied up to the Fermi energy:

$$E_F = \frac{\hbar^2 \cdot k_F^2}{2m} \geq E_{n_x, n_y} = \frac{\hbar^2 \cdot k_{n_x, n_y}^2}{2m} = \frac{\hbar^2 \cdot (n_x^2 + n_y^2) \cdot \pi^2}{2m \cdot W^2} \tag{15}$$

The highest energy level occupied correspond to $n_M = n_x = n_y$. $n_M^2 = M$ levels are occupied. From Eq.15 it is therefore deduced that:

$$M = \text{int} \left[\frac{k_F^2 \cdot W^2}{2\pi^2} \right] = \text{int} \left[2 \frac{W^2}{\lambda_F^2} \right], \tag{16}$$

with $k_F = 2\pi/\lambda_F$. The number of modes is directly proportional to the area W^2 of the cross-section of the wire and therefore to the number of atoms in the cross-section. Moreover, M depends also on the transverse energy of the electrons traveling along the wire.

4.4 Tunnelling junction and Simmons' model

When the electromigration process is over, in an ideal case, two electrodes are formed, separated by a gap, with a width approximately between 1 nm and 2 nm. In this condition, a tunnelling current is measurable. A drop of the current level of 2-3 orders of magnitude is observed when the last atom connecting the two side of the bridge migrates. Tunnelling current can be modeled starting from Landauer-Büttiker formalism [42]:

$$I(V) = \frac{2e}{h} \int_0^\infty [f_L(E) - f_R(E)] \cdot \sum_{i=1}^N T_i(E, V) dE, \quad (17)$$

with f_L and f_R the Fermi distributions of electrons in the left and right electrode, N the number of conducting channels and $T_i(E, V)$ the probability that an electron, with a total energy E when a bias V is applied, tunnels through the barrier. For a single conducting channel, Eq.17 can be simplified to :

$$I(V) = \frac{2e}{h} \int_0^\infty [f(E) - f(E - eV)] \cdot T(E, V) dE, \quad (18)$$

where, according to the Wentzel Kramers Brillouin WKB approximation, the transmission probability $T(E, V)$ can be expressed as:

$$T(E, V) = \exp\left\{ - \int_0^s \frac{4\pi}{h} \sqrt{2m[\phi(z, V) - E]} dz \right\} \quad (19)$$

Here $\phi(z, V)$ is the potential profile along the barrier and s is the coordinate in the barrier where $\phi(z, V) - E = 0$. If this condition is never met, then $s=d$, where d is the width of the nanogap. The potential barrier, with a first approximation, can be considered as a tilted trapezoid. In this case $\phi(z, V) = \phi_L + (\phi_R - \phi_L - eV) \cdot \frac{z}{d}$.

A more comprehensive approach would include the image potential for the determination of the shape of the barrier along the gap. Image potential reduces the thickness of the barrier and rounds off the corners, thus increasing the predicted transmission probability of electrons through the barrier for a given bias. In Eq.19 $\phi(z, V)$ would no longer be a simple linear relation and the limits of integration would be s_1 and s_2 , the two coordinates where $\phi(z, V) - E = 0$.

A set of modifications can be implemented in this model, in order to simplify the equations for some specific regimes of operation. Simmons [45] has identified three ranges of voltage applied, which leads to three equations to compute the current density through a barrier when a positive voltage is applied to the right electrode. In the following equations, a tilted trapezoidal barrier, with a vacuum gap, is considered.

For voltages lower than ϕ_L ($0 < V < \phi_L$) the $I(V)$ characteristic is linear. The current density is expressed as:

$$J(V) = 3.16 \cdot 10^{10} \cdot \phi_L^{(1/2)} \cdot \frac{V}{d} \cdot \exp\left(-1.025 \cdot d \cdot \phi_L^{(1/2)}\right) \quad (20)$$

In the high voltage range, namely when $V > \phi_L/e$, the junction enters the Fowler-Nordheim regime. The barrier has a triangular shape and the characteristic is exponential.

$$J(V) = 3.38 \cdot 10^{10} \cdot \frac{V^2}{d^2 \phi_L} \cdot \left\{ \exp\left(-0.689 \cdot \frac{\phi_L^{(3/2)} d}{V}\right) - \left(1 + \frac{2V}{\phi_L}\right) \cdot \exp\left[-0.689 \cdot \frac{\phi_L^{(3/2)} d}{V} \cdot \left(1 + \frac{2V}{\phi_L}\right)\right] \right\} \quad (21)$$

In the intermediate voltage range $V \simeq \phi_L$ and the current density is highly non-linear. $J(V)$ can be expressed as a linear combination of products of exponentially and linearly dependent terms.

When a negative voltage is applied to the right electrode, the three regimes and equations are still valid, substituting V with the absolute value $|V|$ and ϕ_L with ϕ_R .

4.5 Reduced work function

In the devices studied in this work, the electrodes material is gold. The work function of bulk gold is 5eV. However using this value for ϕ_L and ϕ_R would lead to wrong estimation of the gap width. It has been proved that the work function of gold electrodes, created after electromigration is often lower than 1eV [42]. Two factors that contribute to this effect are the presence of defects on the surfaces and the adsorption of impurities from the environment. Due to the latter issue, an ideal metal-insulator-metal is not feasible if the whole process is not performed under ultra-vacuum conditions. Non-linearity at low voltage after exposure to air of the electrodes, which is explained by a low work function, has been demonstrated [46]. Moreover theoretical works prove that adsorbates, for example Cu, can lower the work function of metals [47].

Generally the two electrodes have two different work functions. Thus the junctions have an asymmetric $I(V)$ curve.

5 Experimental setup

5.1 Mechanical probe station

The devices are characterized and electromigrated with a semi-automatic probe station (Cascade Microtech Summit 12000 Semi-Automatic Wafer Prober). This tool allows to use 4 probes (SMU1, SMU2, SMU3, SMU4) which can be biased to a specific voltage or current level and at the same time measure both the voltage and the current level. Two probes (SMU1, SMU2) are connected to a preamplifier, which in turn is connected to a Keithley 4200-SCS characterization system. As a consequence, the noise level of these two probes is $I_{noise} \simeq 50 \text{ fA}$, while the remaining two probes (SMU3, SMU4), which are directly connected to the Keithley, have noise level $I_{noise} \simeq 10 \text{ pA}$. Through the Keithley 4200-SCS, the user can set the bias of the probes and decide which physical values have to be measured.

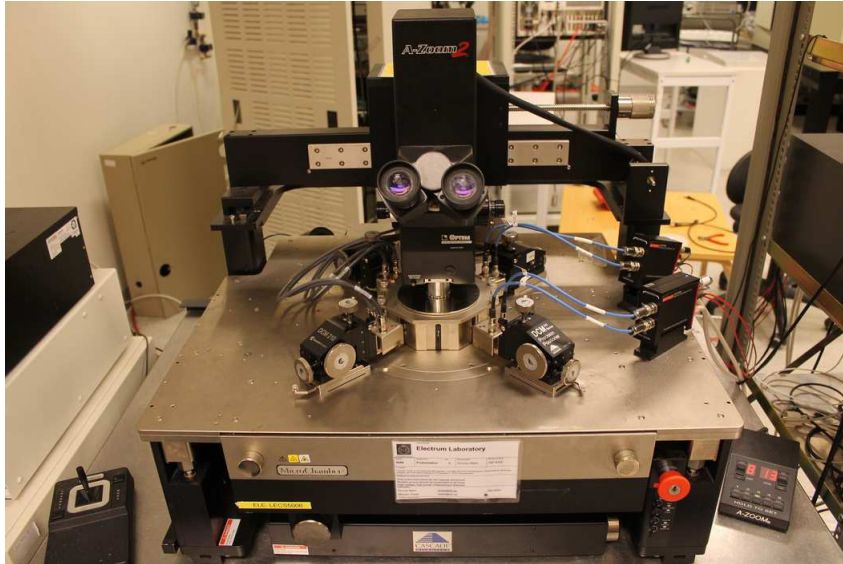


Figure 12: Mechanical probe station used for electromigration and characterization.

A four-points measurement is adopted: a fixed voltage is applied between two probes, while the remaining two probes measure the relative voltage difference, allowing ideally no current (infinite resistance approximation in the electronic circuit connecting the two probes). This method allows to separate the contribution of contact resistance from the value of the bridge resistance, since the large current induced by the voltage applied does not flow through the two needles in charge of measuring the voltage drop between the two electrodes.

Furthermore, the value of the contact resistance ($R_{cont} \simeq R_{2p} - R_{4p}$, see Tab.1) can be deduced before the beginning of the electromigration. For an optimal electromigration a key requirement is a low value of contact resistance, so that heat dissipation is minimized [40], leading to a more controllable and reproducible process.

The semi-automatic probe station allows two modes of operation, namely a manual mode and a semi-automatic mode. In the manual mode, the probes are position over the pads manually, through knobs or a dedicated software. Each measurement

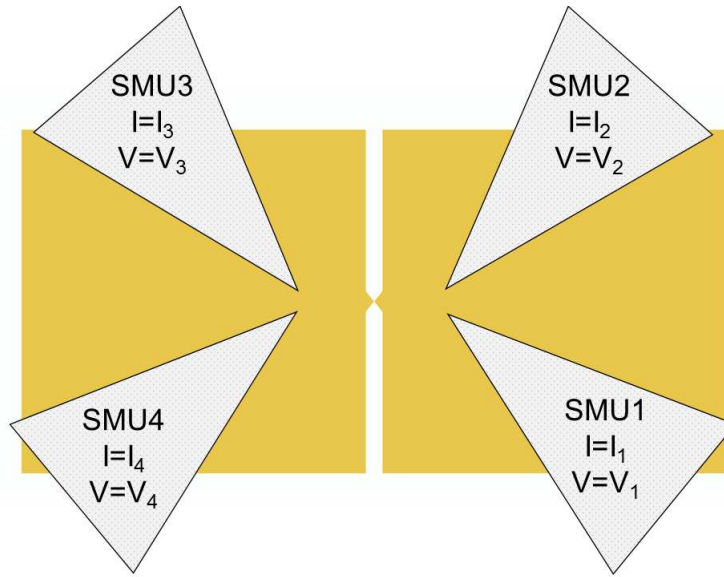


Figure 13: Illustration of the 4 probes measurements, with the names of the current and voltage for each probe used in this work. SMU1 and SMU2 are connected to a preamplifier and allow low current measurements. SMU4 was biased at $V_4=0$ V and SMU1 was set at the desired bias level. No current was allowed through SMU2 and SMU3 ($I_2=I_3=0$ A).

Parameter	Mathematical formula
R_0	$h/2e^2 \simeq 12.9 \text{ k}\Omega$
G_0	$2e^2/h \simeq 77 \mu\text{S}$
R_{2p}	V_1/I_1
R_{4p}	$(V_2 - V_3)/I_1$
R_{cont}	$R_{2p} - R_{4p}$
G_{2p}	I_1/V_1
G_{4p}	$I_1/(V_2 - V_3)$
$G_{2p,norm}$	$G_{2p}/G_0 = R_0/R_{2p}$
$G_{4p,norm}$	$G_{4p}/G_0 = R_0/R_{4p}$

Table 1: Summary of the parameters used in this work, along with their mathematical formula.

has to be launched by the user. In the semi-automatic mode, a reference point in a reference die is set. The tool can then move automatically in different dies and/or different locations (subsites) within the die, manually inserted in the software. Once the probes are moved to the selected location, a set of measurements is performed. At the end of the automatic measurement, a single file containing all the data collected is automatically saved. The semi-automatic mode in this work is used only for statistical purposes, for example for the collection of the initial resistance of the bridges over the whole sample.

During the process of electromigration, due to issues of minimization of contact re-

sistance and not perfectly sharp tips, which makes challenging to have a good contact of the four probes to the two pads, the probes were carefully positioned manually. Then a first measurement was launched, with a low voltage (in the range of 50 mV - 100 mV) that prevented the onset of electromigration. Since the manual mode software shows in real time the results of the measurements, it was possible to check the difference between the value of R_{2p} and R_{4p} . The difference between the two is approximately the contact resistance R_{cont} (see Tab.1) of SMU1 and SMU4. If the difference was considerably larger than the average value ($\sim 20 \Omega/30 \Omega$ depending on the sample), the probes were positioned again. When the contact resistance reached a satisfying value, the electromigration process was launched. Generally the process consisted in applying a fixed voltage to the probe SMU1 (V_1), while $V_4=0$ V. The two remaining probes (SMU2, SMU3) measured the voltage drop between the two extremities of the electrodes, while not allowing a current through them ($I_2=I_3=0$ A), to avoid the contribution of the contact resistance. To conclude, the voltage applied to SMU1 correspond to the voltage difference $V_1 - V_4$. In the following, this voltage difference will be referred to as V if not differently specified ($V=V_1=V_1 - V_4$). It has to be noted that part of this voltage difference drops on the contact resistances, so the effective voltage applied to the extremities of the bridge is lower.

Avoiding the contact resistance contribution in the measurements has been proved to be a necessary requirement during the experimental sessions. Contact resistance value can vary during the measurement, due to microscopic movements of the needles or reconfiguration when a current flows through the needles. Fig.14 shows an example of variation of the contact resistance over time.

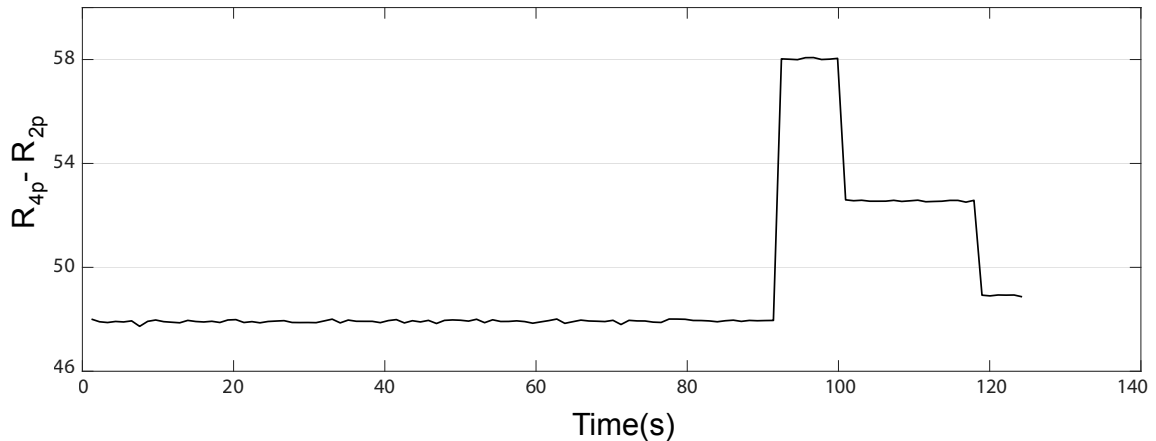


Figure 14: $R_{4p} - R_{2p} \simeq R_{cont}$ varies over time when the anti-vibration platform holding the probe station is hit with the operator hand. In this image, the 3 clear steps correspond to 3 hits, where only R_{2p} changes, while R_{4p} is not varying.

In this case, the anti-vibration table on which the probe station was placed was hit by the operator. As a consequence of each hit, the contact resistance abruptly changes and the resistance R_{2p} jumps to a new stable state. On the contrary the resistance R_{4p} is not affected by the hits, proving that the bridges have a good mechanical stability and are not affected by mechanical vibrations. The variation of the value of R_{2p} has

been explained as the result of microscopic movements of the needles induced by the hits. The jumps in R_{2p} occurred also pressing the keys of the light-controller of the optical microscope, visible on the right of Fig.12, and by accidentally bumping into the anti-vibration table. These jumps could be erroneously attributed to conductance steps seen during electromigration due to ions migration in the ligaments. Moreover during some electromigration processes a random variation of R_{2p} was observed, without any induced vibrations. These variations were particularly visible during the first seconds of the procedure and can be explained by atomic rearrangement in the region of the needles-pads interface due to the current flow. As a consequence 4 probes measurements during electromigration were necessary and were always performed for the collection of the data presented in this work.

6 Results and discussion

In this chapter the results of the experimental measurements are introduced and discussed. Each section focuses on one of the 4 samples available and describe the typical electromigration process observable, along with statistical results and considerations about the influence that several parameters have on the process. The sequence of the sections follows in large part the chronological succession of the experiments, since each new set of measurements is planned according to the previous results.

6.1 Preliminary tests on 1b

The first set of measurements has been performed on the sample 1b, which contained 2 available dies. Due to a not perfect cleaving process that cut out some junctions and since some measurements were performed previously on some junctions, not all the devices could be used. A total number of 94 devices could be investigated, of which 42 were in the column S3 and 52 in the S2 column.

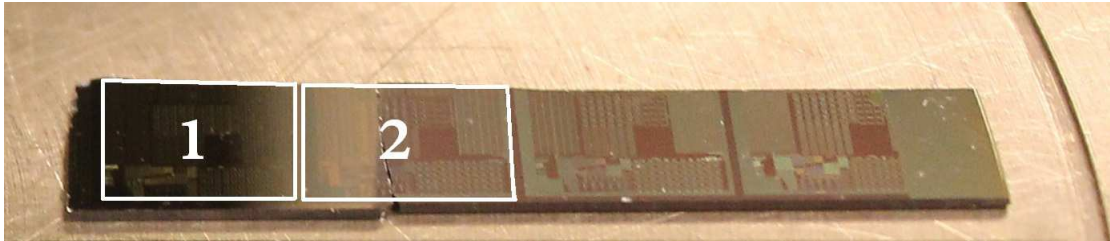


Figure 15: Sample 1b with the numeration of the dies used.

Firstly, a two-probe statistical analysis has been carried out, to establish the number of useful devices for the electromigration process amongst the 94 available. The analysis consisted in applying a low voltage, in this case 100 mV, and measuring the current response. The obtained conductance was then normalized to the conductance quantum.

$$\frac{G}{G_0} = \frac{I}{V} \cdot \frac{h}{2 \cdot e^2} \quad (22)$$

If this dimensionless number is larger than 1, then there is a conductive path between the two pads, that is to say one or more ligaments connect the two sides of the bridge. When this figure is lower than one, a gap separates the electrodes and the device cannot be used for the electromigration process investigation.

77 connected devices were found, among the total 94 measured (82%).

6.1.1 Minimum breakdown voltage and typical electromigration

Then a first preliminary study followed, in which the main goal was to find the minimum voltage capable of starting electromigration. The procedure consisted in applying a fixed voltage, as low as 1 mV, for a maximum time of 5 min, and in case of

no observation of electromigration effects, the voltage was then increased. The minimum voltage capable of triggering electromigration was found to be $V = 150$ mV. Fig.16, 17 and 18 display the complete process of electromigration for a breakdown voltage $V=150$ mV and represent an excellent example to discuss some of the features of the electromigration procedure under investigation in this thesis. This device belonged to column S1 and is the only one of this kind discussed in this work, all the other devices being in S2 or S3 column. However the process contains all the typical features observable in the other 2 columns in sample 1b.

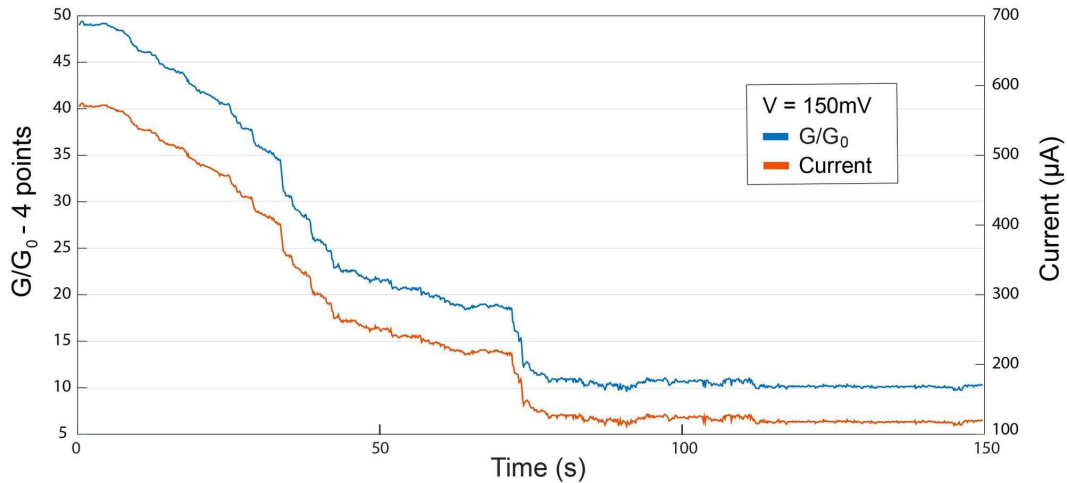


Figure 16: First measurement at 150 mV, showing the beginning of the electromigration process. When a fixed voltage is applied, the increase of resistance brings about a decreasing current, preventing catastrophic effects at the moment of the breakdown due to the intolerable current density in a nanometric constriction.

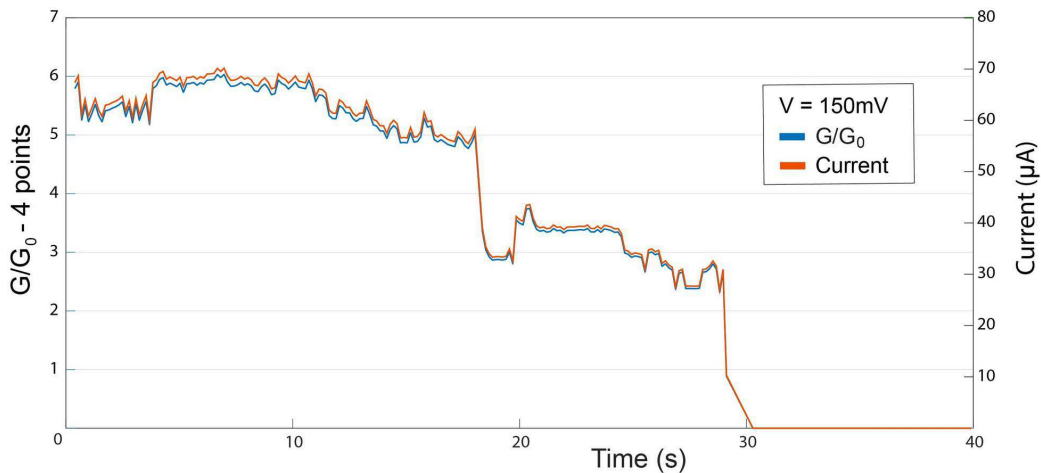


Figure 17: Second measurement at 150 mV with the final part of the electromigration process. The initial conductance is lower than the final one of the first measurement, suggesting that atomic rearrangement has taken place between the two measurements. Steps of conductance can be observed before the breakdown, with the last data point collected at $1 \cdot G_0$.

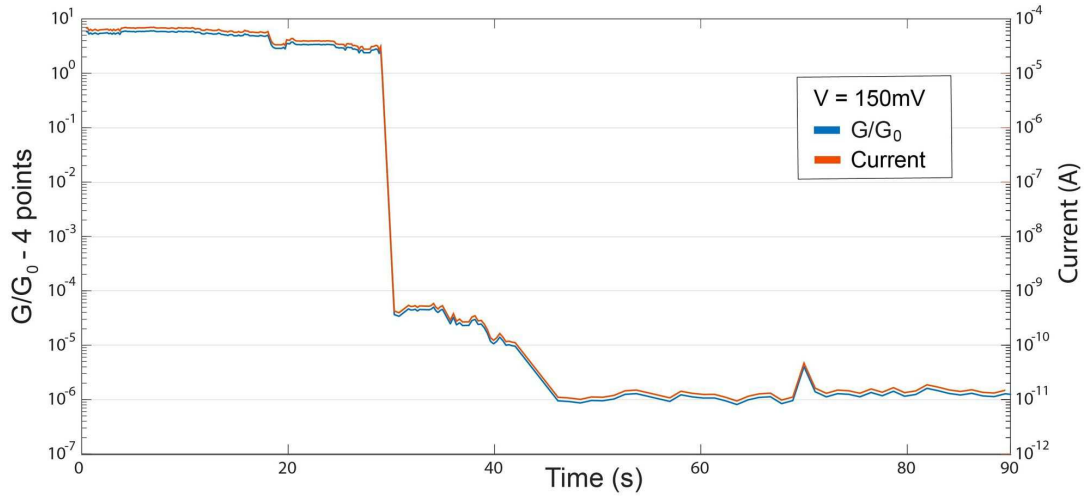


Figure 18: Second measurement at 150 mV with the final part of the electromigration process, plotted with a logarithmic scale. Here it is visible the conductance reduction of more than 4 orders of magnitude ($2.4 \cdot 10^4$ precisely) at the moment of breakdown.

It has to be noted that prior to the onset of electromigration, other measurements were performed, increasing progressively the voltage from 1 mV to 150 mV every time a new measurement was launched. Precisely, an aggregate measurement time of ~ 15 min was performed before the data plotted in the previous graphs were collected. This could have affected the measurements carried out at 150 mV, due to atomic rearrangement of the ligaments when a lower bias is applied for a long time. Furthermore two distinct measurements are performed with the same applied voltage here, while a single one is preferable and is the common practice. Current spikes at the beginning of the measurement and cooling of the bridge when the voltage is interrupted could lead to atomic rearrangements in the ligaments and so they should be minimized. These effects play a major role particularly when the ligaments are narrowed down to a cross section of few atoms, approximately when $G < 10 \cdot G_0$, inducing an unbearable current density or an instability in the structure due to thermal effects. However it shows common features of a successful electromigration process in the sample 1b.

When the voltage is applied the conductance gradually decreases. Gold atoms are moved away from the ligaments and flow towards the positively biased electrode. No clear steps are observable in this starting phase. The cross section of the ligaments contains a number of gold atoms in the range of tens and hundreds of units. The gold atoms on the surface of the ligaments are the most weakly bound and so they are the most likely to be moved away from the ligaments by the electron wind force [43]. A larger step is visible in Fig.16 between 70 s and 80 s. It is assumed that a cluster of atoms leaves the ligament at the same time.

In the second measurement at 150 mV (Fig.17) the starting conductance is equal to $6 \cdot G_0$, while at the end of the first one was stable at $10 \cdot G_0$. As already mentioned in this section, atomic rearrangements can take place between two measurements and lead to a different starting condition at the beginning of the following one. Once a sub- $10 \cdot G_0$ is reached, big change in resistance are observable every time an atom

moves from the ligament, leading to a different conduction scenario between the two sides of the bridge. Some conductance levels are visible in Fig.17 at $6 \cdot G_0$, $5 \cdot G_0$ and $3 \cdot G_0$. Finally the structure is very unstable and the breakdown of the bridge occurs. The process is very fast and the rate of data collection could not allow observing the last steps (only one data point is collected at $1 \cdot G_0$).

As shown in Fig.18, the conductance drops abruptly, with a $2.4 \cdot 10^4$ -fold reduction between two collected points (1.1 s between the two points). This is a clear indication that the last atom bridging the two electrodes is moved away and that a different transport mechanism takes place. A nanogap is created and quantum tunnelling allows measuring a current, in a range between 1 nA and 10 pA. The tunnelling current is not stable immediately after the breakdown. Thermal effects and the high electric field could promote atomic rearrangements, increasing the size of the nanogap. Finally the current reaches a stable value at 10 pA.

To conclude, the whole process took 3 min, which is consistent with other electromigration measurements in the sample 1b, lasting generally in a range between 1 min and 10 min. The process led to the formation of a nanogap, where a tunnelling current of 10 pA at a relatively low bias is measurable. Thus the tunnelling resistance at 150 mV is 15 G Ω , which is in line with other results reported in literature [48].

6.1.2 Investigation of electromigration protocol

In sample 1b, 18 devices were tested applying a fixed voltage as low as 100 mV and increasing it when the electromigration process did not start in the first few minutes. All devices created a nanogap and a tunnelling current could be detected after the breakdown. Tab.2 summarizes the results.

9/18 (50%) devices needed a voltage $V \leq 200$ mV to form a nanogap. Only 3/18 (17%) needed $V \geq 300$ mV, and in those cases the voltage required to create a gap was considerably higher, specifically 700 mV, 1 V and 1 V. When such a high voltage is applied at the moment of the breakdown, generally tunnelling current are feeble and can be measured only sweeping the voltage to high values, in the range of 5 V. The behavior is exponential in this range and the linear region can not be measured, since the tunnelling current is below the noise level of the probestation, around ~ 50 fA.

The breakdown voltage does not show a clear dependence on the initial conductance of the ligaments. However a low breakdown voltage is observed only for low initial values of $G_{4p,norm}$. Indeed $V \leq 175$ mV is sufficient to create a gap only for $G_{4p,norm} \leq 50$. Using a low voltage, the electromigration process is generally gradual and conductance steps are observed before the breakdown.

Generally the whole electromigration process lasted in a range from 1 min to 10 min when the voltage was relatively low, $V \leq 250$ mV. Hillocks formation was only observed when a large breakdown voltage $V \geq 300$ mV was applied for a time longer than 10 min. Thus hillocks were observed rarely and only in extreme conditions, suggesting that the devices in sample 1b are robust against this phenomenon. As it will be reported in the next sections, hillocks formation occurs more frequently in the other samples, often hindering nanogap formation.

These results display a promising behavior of electromigration in crack-outlined lig-

aments. The voltage range needed for the creation of the nanogap is quite narrow, since in most of the devices (15/18) a voltage lower or equal to 300 mV is sufficient. A tunnelling current is generally detected at low bias, demonstrating the formation of a gap narrower than 3 nm. Taking into consideration the required voltage for nanogap creation, tunnelling current detectability, hillocks formation and time needed for the process, an optimal voltage in a range from 200 mV to 300 mV can be assumed, applying the voltage for a maximum time of 10 min. With this optimal voltage, the yield of nanogap formation starting from ligament(s) bridging the Au electrodes, based on the result discussed in this subsection, can be hypothesized to overcome 80%.

Device #	Design	Breakdown V	Initial $G_{Ap, norm}$
1	S1	150 mV	50
2	S2	1 V	15
3	S2	250 mV	50
4	S2	200 mV	101
5	S2	175 mV	34
6	S2	200 mV	68
7	S2	200 mV	115
8	S3	300 mV	90
9	S3	200 mV	60
10	S3	250 mV	95
11	S3	225 mV	82
12	S3	175 mV	36
13	S3	220 mV	103
14	S3	700 mV	72
15	S3	1 V	93
16	S3	300 mV	115
17	S3	200 mV	99
18	S3	200 mV	42

Table 2: Summary of the electromigration investigation in 18 devices in sample 1b. Here are reported the voltage needed to create the nanogap in each device, along with the design and the initial normalized conductance before the electromigration process.

6.1.3 Conductance below conductance quantum

Another typical feature of sample 1b is the observability of conductance levels below $1 \cdot G_0$ before nanogap formation in a large fraction of devices, around $\sim 20\%$. This phenomenon is still compatible with the ballistic theory introduced in this thesis. According to Eq.13 sub- G_0 conductance is possible when the transmission probability T is lower than one, i.e. in a non ideal case. This is a common feature in electromigrated nanogap junctions. However the other samples analyzed in this thesis did not show sub- G_0 with a frequency comparable to that of sample 1b. This feature in

part is attributed to the relatively low voltage needed to observe the onset of electromigration, which allows a gradual and slow process. Nevertheless sub- G_0 steps are observable also for relatively high voltages, i.e. 300 mV, representing a clear difference with the other samples, which show often quick processes that do not allow measuring the final steps before breakdown. For example, in the 18 devices introduced in subsection 6.1.2, only in one device a gap was formed before that a first data point was collected. As shown in the following sections, this trend is reversed in other samples.

Fig.19 shows the breaking of a ligament, with the last conductance plateau at $0.1 \cdot G_0$. A voltage equal to 250 mV was applied and stopped when the conductance reached a value lower than $5 \cdot G_0$. Then a low voltage $V = 100$ mV was applied, allowing for a slow or negligible gold atoms electromigration. Sharp steps are visible due to atomic rearrangements of the ligament, in a similar fashion of nanogaps obtained with self-breaking of nanowires [26]. Steps at approximately $4 \cdot G_0$, $3 \cdot G_0$ and $2 \cdot G_0$ are observed. A last conductance level at $0.1 \cdot G_0$ is measured. A possible explanation of this phenomenon is that the transmission probability was close to ideal with multiple atoms, but with one atom bridging the electrodes, the atomic arrangement was such that $T < 1$.

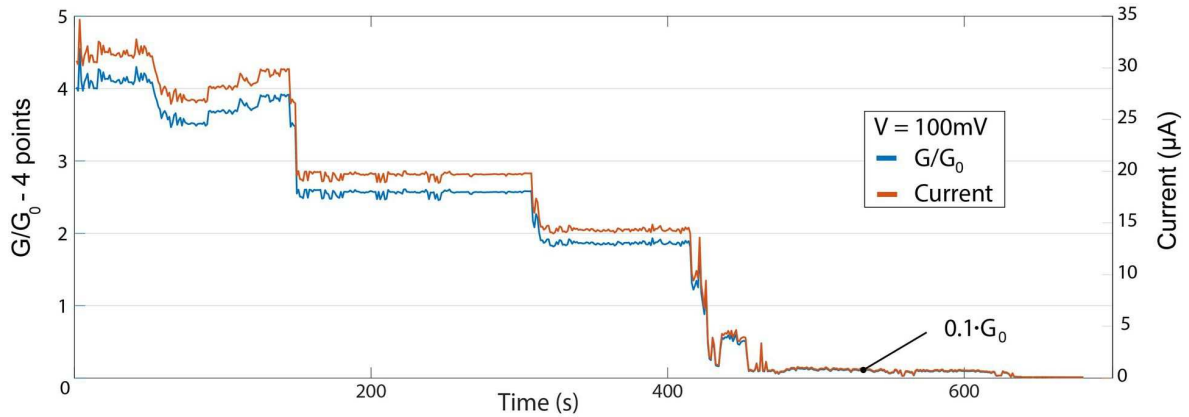


Figure 19: Conductance steps before breakdown, with a last level at $0.1 \cdot G_0$. The low voltage V applied allows for a slow process, enabling to see all the conductance plateaus.

6.1.4 Final considerations on 1b

Sample 1b shows often optimal electromigration processes leading to a successful formation of a tunnelling nanogap junction. Here is reported a list of features of this sample:

- relatively low breakdown voltage, with 50% of the devices creating a nanogap with a voltage $V \leq 200$ mV;
- gradual decrease of the conductance, with steps clearly visible before the breakdown;
- sub- G_0 conductance steps visible in around 20% of the processes;

- tunnelling current after nanogap formation measurable in all devices, even if few times (3/18) voltage had to be raised to 5V to observe it;
- tunnelling resistance at low bias between 50 M Ω to 25 G Ω . Sometimes the linear regime could not be measured since the current was lower than the noise level;
- few hillocks formed, limited to the processes involving an high voltage applied, $V \geq 300$ mV for a long time, namely more than 10 min.

A characteristic electromigration process is illustrated in Fig.20. A relatively low voltage (200 mV) is needed to start electromigration and to create the nanogap. The conductance decreases gradually in a couple of minutes, with some discrete steps, particularly visible before the breakdown. Final steps are at a low conductance value, in this case at $1 \cdot G_0$. The process leads to the creation of a tunnelling nanogap junction, with a linear resistance at low bias of 700 M Ω . The fit of the $I(V)$ tunnelling curve, implemented with an asymmetrical barrier model, returns a gap width of 0.88 nm. (See Appendix 3 for the details of the fit).

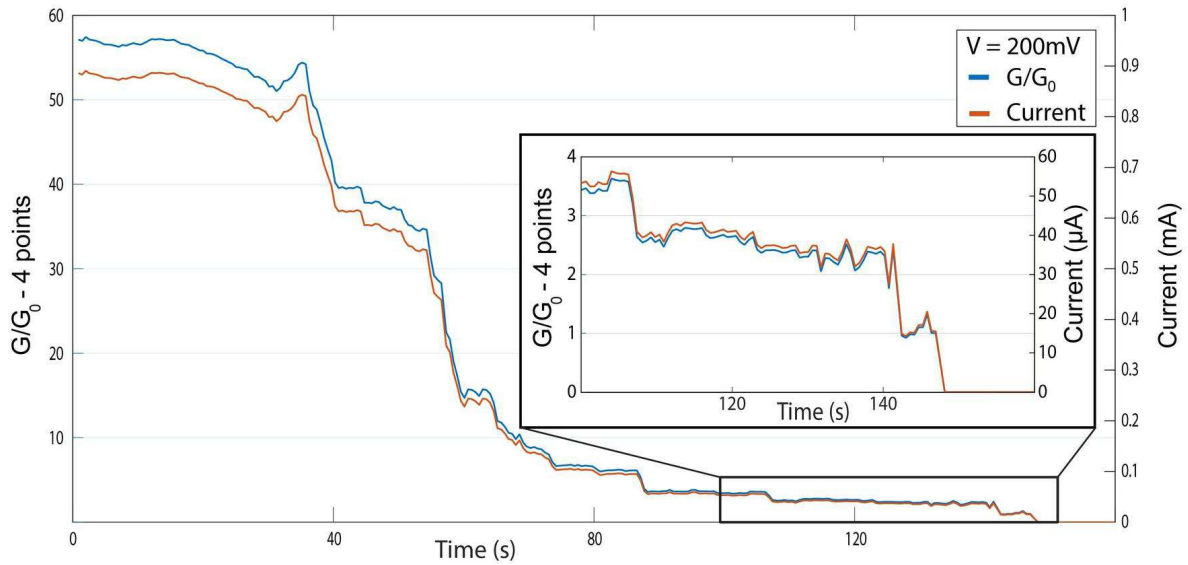


Figure 20: Complete electromigration process of a device in column S3 of sample 1b. The inset shows the last part of the process before breakdown.

6.2 Large statistical analysis on 1a

Sample 1a was analyzed after 1b. It has to be remarked that the two samples differ from each other only in the post-processing procedure, which for the sample 1a consisted in two series of 1 min of Oxygen plasma etching in ICP, whereas for 1b only 1 series of 1 min was performed. This post-processing step was aimed at etching away the residual of organic material (e.g. resist) from the surface of the junctions. The electromigration process is very sensitive to the surface structure. In addition to potentially modify the electromigration process, organic residual can influence the

behavior of the nanogap, for example bridging the two electrodes. For these reasons, working with a debris-free surface is a strict requirement.

6.2.1 Resistance distribution

Sample 1a consisted of 29 usable dies, for a total number of 870 devices in the S2 columns and just as many in the S3 columns. Firstly a statistical analysis with the semi-automatic probe station was performed, in order to map the bridged devices and determine the large-scale distribution of initial resistance. Tab.3 displays the fraction of devices connected through ligaments in the two columns S2 and S3 over the whole wafer.



Figure 21: Sample 1a with the numeration of the dies used.

	Columns S2	Columns S3
Devices with ligaments	482/870 (55.4%)	509/870 (58.5%)

Table 3: Number of devices in the sample 1a which showed bridged pads. The criteria for determining the presence of the ligaments was that the conductance was larger than the conductance quantum ($G > G_0$).

The designs in the two columns show a similar behavior. Besides having a comparable percentage of bridged devices (between 55% and 60%), they show comparable average values and distribution within each die. However these values greatly vary moving from the edges of the wafer to the center. In particular, in the center of the wafer a larger fraction of devices is bridged and the mean value of resistance is lower. Around 80% of the devices is bridged in the most central dies indeed, with a maximum of 54/60 (90%) in the die #23. On the other hand, around 40% of the devices in a die near the edge shows a conducting path between the pads, with a minimum of 17/60 (28%) in the die #1. Also the distribution of the resistance is affected by the location of the dies. Fig.22 shows the distribution of the resistance in 12 dies close to the edge and 6 dies in the center of the wafer. The mean value of the resistance measured for the devices in the central part of the wafer is 185.7Ω , while

in the periphery of the wafer the average value is 64% higher, namely 303.7Ω . The latter number is mainly due to a larger spread of values in the high resistance range, while in the central dies the distribution of resistance is considerably narrower, as illustrated in Fig.22.

The variation is due to non-uniformities over the wafer during the fabrication processes. In particular, the etching rate of the sacrificial layer (a-Si) is higher at the edge of the wafer. This implies that a larger portion of the TiN-Cr-Au stack is released, experiencing a larger stress and a larger gap in the TiN layer according to Eq.1. Thus the pulling action at the edge of the wafer on the gold layer is larger as well, producing a larger number of devices with a gap already present. The distribution of resistance is also shifted to higher values, having on average narrower ligaments, and a smaller number of them.

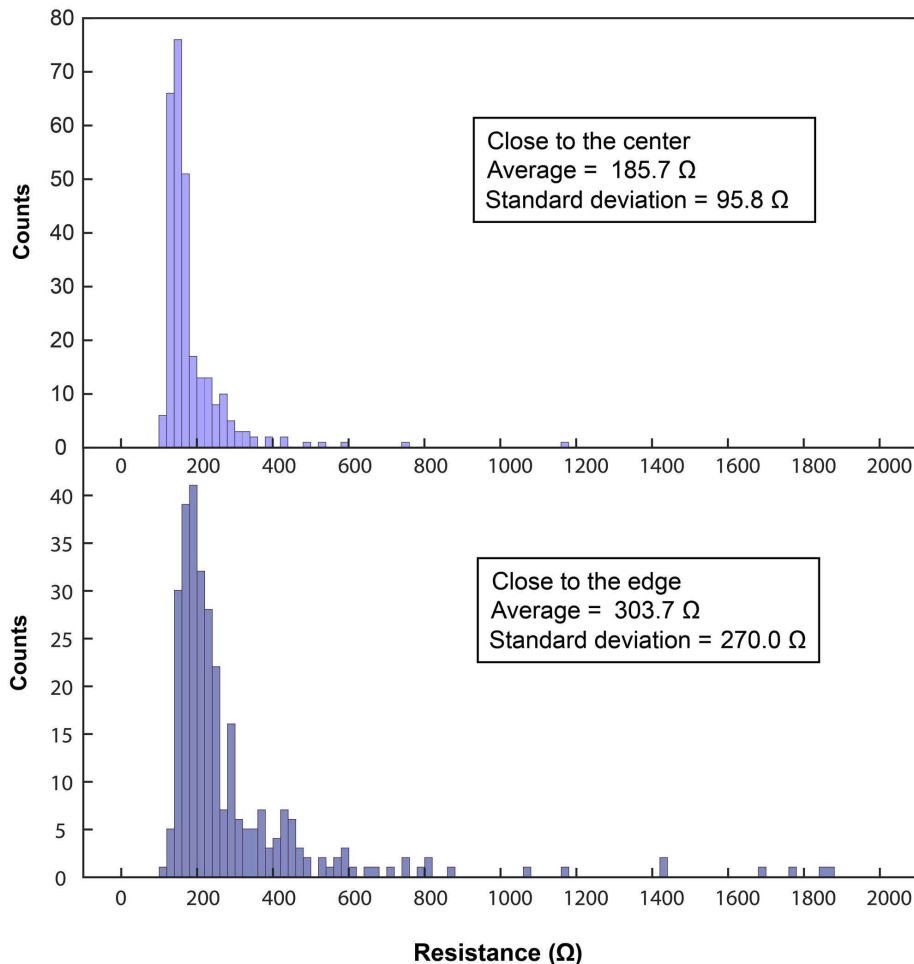


Figure 22: Distribution of the resistance in the sample 1a. The upper figure shows the histogram of the distribution on the dies at the edge of the wafer (296 devices, dies 1-2-3-4-7-8-12-13-18-19-24-25), while the bottom figure is related to dies at the center of the wafer (282 devices, dies 21-22-23-27-28-29). Both graphs have bin size of 20Ω .

6.2.2 Analysis of electromigration: part 1

A more systematic approach was adopted for the investigation of the electromigration process in sample 1a. Through the map of the initial resistance over the whole sample, 25 devices were analyzed in the S3 columns of different dies. 3 voltage values were selected, based on the results obtained with sample 1b. The 3 levels are 200 mV, 225 mV and 250 mV. For each voltage level, a set of devices within the 25 was chosen, taking care to pick them in a wide range of resistance.

The electromigration protocol consisted in applying the selected fixed voltage for a time of 15 minute. If a nanogap was formed before the time limit, the voltage was stopped when the tunnelling current reached a stable level. In these cases a low voltage sweep, from -0.2 V to 0.2 V , was then performed and the resistance in the linear regime was extracted. The results of the measurements are reported in Tab.4. This results differ greatly from the ones found in the sample 1b. Here the electromigration process can develop in two opposite ways. Either the process leading to the creation of a gap is quick, few seconds generally, or the process of electromigration starts but slows down and stabilizes to a certain level of conductance. Moreover the yield is lower, creating a nanogap in 11 devices out of 25 (44%). However only in 6 of them a tunnelling resistance fitting could be performed with low bias sweep, from -0.2 V to 0.2 V . Increasing the voltage sweep range could have led to a measurable tunnelling current in a larger fraction of devices, but in this case it was avoided since it was observed in other devices in sample 1a and 1b that an high voltage can cause atomic rearrangement at the nanogap tips, probably due to the extremely high electric field in the nanogap. Thus the measured tunnelling current could not be associated with certainty to the one relative to the gap formed by the electromigration process. Another feature of this sample is that tunnelling resistance values are generally much higher than those found in sample 1b, in a range between few $\text{G}\Omega$ and few $\text{T}\Omega$. Finally conductance steps could not be generally observed. The conductance decreased steadily with a fast pace in the cases of nanogap formation, while when the outcome was still a connected bridge, the decrease was gradual, reducing its rate over time and eventually reaching a stable level of conductance. The fast electromigration process in the cases of breakdown is probably the major reason for the non-observability of conductance steps, especially at the final stages of the process. Each data point was collected after a current integration typically having a duration in a range from 1 s to 4 s, potentially hindering the measurement of variations in the conductance level taking place in a smaller time scale.

Some considerations can be drawn from the results of the 25 devices analyzed. Firstly, higher voltage applied leads to an higher yield of formation of a nanogap, indeed 29% of devices underwent breakdown with 200 mV, 36% with 225 mV and 62% with 250 mV. From these small set of results a correlation between applied voltage and tunnelling current level after the process can not be observed. Overall, a larger voltage is needed to observe the onset of electromigration and to reach process yield similar to those of sample 1b. Finally, the initial conductance of the bridge seems to have an influence on the outcome of the process, especially with $V=200\text{ mV}$ and $V=225\text{ mV}$. In particular low values of G_{init}/G_0 lead to an higher yield of nanogap formation. This is a reasonable result, since a low conductance

value is related to a narrow ligament, and thus more sensitive to electromigration.

Device #	Voltage	G_{init}/G_0	Time	R_{tun}	Outcome
1	200 mV	70	15 min	/	X
2	200 mV	81	25 s	/	✓
3	200 mV	96	15 min	/	X
4	200 mV	101	45 s	/	✓
5	200 mV	107	15 min	/	X
6	200 mV	107	15 min	/	X
7	200 mV	134	15 min	/	X
8	225 mV	41	15 min	/	X
9	225 mV	51	25 s	180 GΩ	✓
10	225 mV	86	<3 s	8 GΩ	✓
11	225 mV	92	<3 s	12 TΩ	✓
12	225 mV	103	15 min	/	X
13	225 mV	106	<3 s	/	✓
14	225 mV	107	15 min	/	X
15	225 mV	112	15 min	/	X
16	225 mV	117	15 min	/	X
17	225 mV	125	15 min	/	X
18	250 mV	44	21 s	/	✓
19	250 mV	80	<3 s	12 TΩ	✓
20	250 mV	80	15 min	/	X
21	250 mV	96	15 min	/	X
22	250 mV	107	<3 s	2 TΩ	✓
23	250 mV	109	15 min	/	X
24	250 mV	109	<3 s	/	✓
25	250 mV	127	70 s	13 GΩ	✓

Table 4: Summary of the electromigration investigation in 25 devices in sample 1a. G_{init}/G_0 is the initial normalized conductance of the bridge. The column **Time** reports the interval for which the voltage was applied before observing a gap. If Time=15 min, no gap was created. When <3 s, nanogap formation happened before that the first data point could be collected. R_{tun} is the tunnelling resistance at low bias. Not all nanogaps were conducting enough to allow for a resistance fitting at low bias. The **Outcome** column indicates for which device a gap is created after the electromigration process.

6.2.3 Analysis of electromigration: part 2

Since the first results obtained with sample 1a did not show a behavior similar to that of sample 1b, another investigation was carried out to find the optimal voltage for the electromigration process. This investigation did not follow a strict systematic approach. A fixed voltage, starting from a base level of 200 mV, was applied. If the process did not lead to the creation of a nanogap within ~10 min or did not show any substantial change in conductance, the voltage was increased. This increase was

applied for a maximum of two times. Tab.5 reports the results of this investigation, showing only the last and thus higher voltage used.

Device #	Voltage	G_{init}/G_0	Time for breakdown	R_{tun}	Outcome
1	200 mV	40	25 s	/	✓
2	300 mV	50	/	/	X
3	225 mV	58	<3 s	290 GΩ	✓
4	250 mV	64	<3 s	1.8 TΩ	✓
5	250 mV	65	60 s	58 MΩ	✓
6	225 mV	69	21 s	42 GΩ	✓
7	300 mV	70	/	/	X
8	250 mV	74	/	/	X
9	300 mV	75	4 min	/	✓
10	300 mV	82	/	/	X
11	300 mV	85	/	/	X
12	225 mV	89	<3 s	/	✓
13	250 mV	92	/	/	X
14	300 mV	95	/	/	X
15	250 mV	100	12 s	18 MΩ	✓
16	250 mV	100	<3 s	9 TΩ	✓
17	240 mV	101	9 s	/	✓
18	300 mV	105	/	/	X
19	225 mV	110	21 s	14 GΩ	✓
20	225 mV	130	4 s	470 GΩ	✓

Table 5: Summary of the electromigration investigation in 20 devices in sample 1a. G_{init}/G_0 is the initial normalized conductance of the bridge. The column **Time for breakdown** reports the interval for which the voltage was applied before observing a gap. If /, no gap was created. When <3 s, nanogap formation happened before that the first data point could be collected. R_{tun} is the tunnelling resistance at low bias. Not all nanogaps were conducting enough to allow for a resistance fitting at low bias. **Outcome** indicates for which device a gap is created after the electromigration process.

Comparing these results with the previous ones obtained in sample 1b summarized in Tab.2, it is clear the different behavior of the devices in the two samples. On average an higher voltage is needed to create a nanogap. While in sample 1b $V \leq 300$ mV was successful 15/18 (83%), in this sample the yield dropped to 12/20 (60%). Even more drastic is the percentage reduction of successful processes at low voltage, namely with $V \leq 200$ mV, from 9/18 (50%) in sample 1b to 1/20 (5%). As already discussed in the first part of the investigation of sample 1a, the process leading to the creation of a nanogap is either very fast, mostly lasting less than a minute, or it stops at a given level of conductance, often creating hillocks in the region close to the ligaments. A tunnelling resistance at low voltage is not always detectable and has generally an high value, in the GΩ and TΩ range. In contradiction with the general behavior observed in sample 1a, in 2 devices the tunnelling resistance assume a

small value, precisely $58\text{ M}\Omega$ and $18\text{ M}\Omega$ in device #5 and #15.

To summarize, in sample 1a is observed an higher voltage for breakdown, an higher tunnelling resistance at low bias and an lower yield than in sample 1b. Moreover the successful processes are usually fast, hindering the observation of steps, and hillocks are often formed close to the ligaments in a long lasting process. To understand the reasons of this different behavior, further investigations were carried out and are discussed in the sections 6.3 and 6.4.

6.2.4 Two typical electromigration processes

As already discussed in this section, the electromigration processes observed in sample 1a can be divided in two categories. In the first one the process is fast and leads to the creation of a nanogap, generally with an high tunnelling resistance. In the second case, the process is slow and gradual, eventually reaching a stable level of conductance. Often hillocks are formed close to the ligaments in the second case. A graph of a quick electromigration (device #1 in Tab.5) and the related SEM pictures before and after the process are shown in Fig.23. Data points in this graph is collected every 5 s. The process is quick even with a relatively low bias at 200 mV, preventing the observation of conductance steps in the final moments preceding the breakdown. The tunnelling current is too low to allow performing a linear fit of the resistance at low bias. The SEM pictures show that a morphological rearrangement has taken place only in the ligament, creating a gap. The SEM resolution ($\sim 5\text{ nm}$) does not allow measuring the gap width. In the case of a quick process, taking place in less than 1 min, hillocks formation has never been observed.

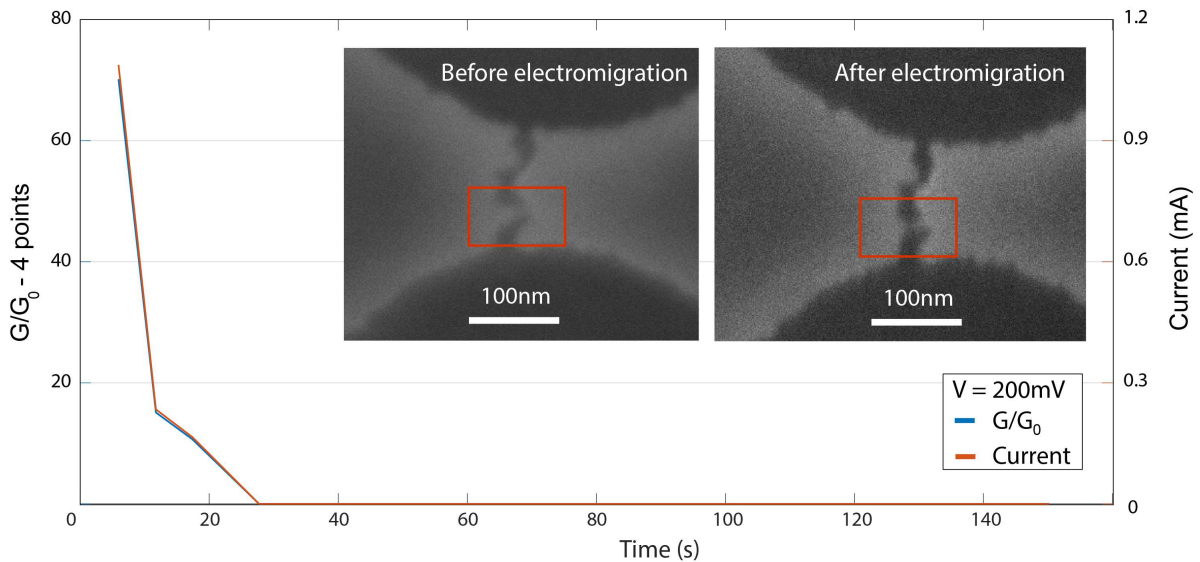


Figure 23: Graph of the electromigration process of device #1 in Tab.5. In the insets are shown the SEM pictures taken before and after the electromigration process. The region affected by the atom migration is highlighted.

Fig.24 shows an example of the second type of electromigration recognized in sam-

ple 1a. A fixed voltage equal to 250 mV is applied for 15 min to the pad on the right of the figure. The process is gradual and slows down over time. In this case in the last 10 min the conductance has a total decrease lower than $2 \cdot G_0$, less than the 3% of the initial conductance. Gold atoms migration involving the ligament however takes place, as it is demonstrated by the growth of hillocks close to the ligament. The formation of these structures takes place always on the side of the bridge on which the positive voltage is applied, making it consistent with an electromigration related phenomenon. The electron wind force indeed act in the direction of the positive voltage side and moves the gold atoms in that direction. Hillocks growth has been observed only for long electromigration processes, with a voltage applied for at least for 5 min, and generally is related to the employment of high voltages. The gold atoms forming the hillocks probably come from the left side of the bridge. Often superficial rearrangement of the left electrode has been observed with SEM. In particular surface smoothing is the most frequent feature in sample 1a. The origin of this phenomenon is not yet clear. Grain structure and in general surface morphology are expected to play an important role in the dynamics of gold atoms migration and accumulation in hillocks. It has been hypothesized that gold atoms migrate along the surface from the left electrode to the right electrode and find an energetically convenient state accumulating in structures on the positively biased side. Unfortunately an extensive literature on this topic is not yet available and further investigations are needed to understand in which conditions this phenomenon is triggered and how can it be avoided.

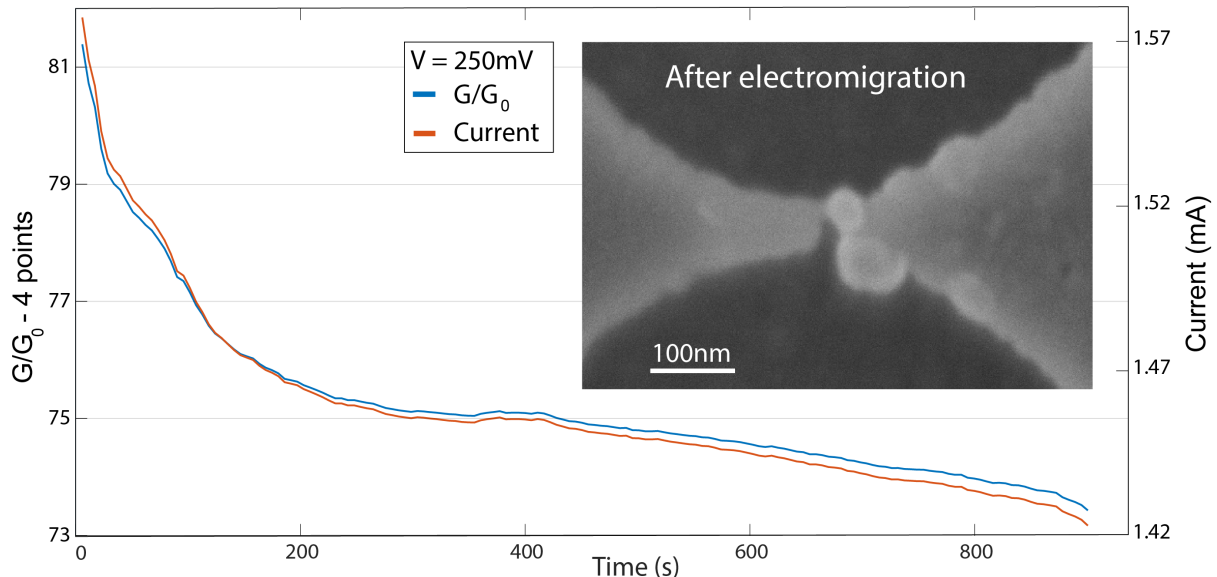


Figure 24: Graph of the electromigration process of device #20 in Tab.4. In the inset is shown a SEM picture taken after the electromigration process. Hillocks close to the ligaments are clearly visible.

6.2.5 Final considerations on 1a

Sample 1a shows a clearly different behavior than sample 1b. Here it is reported a list of features of this sample:

- relatively high breakdown voltage, with a voltage of 300 mV required to overcome the 50% yield of formation a nanogap starting from ligament(s);
- two opposite developments of electromigration: in one case the process is fast, without observable conductance steps, and in the other the process is slow and gradual, stopping at a certain conductance level;
- sub- G_0 conductance levels have never been observed. The high speed of the process hinders their detection;
- tunnelling current at low bias after nanogap formation is not always detectable in all devices. If detectable, generally it displays an high resistance, in a range between 10 G Ω and 10 T Ω ;
- when hillocks grow, nanogaps are never formed;
- hillocks are often formed during a process lasting more than 5 min. These structure grow on the positively biased side of the ligament, giving a further proof that hillocks are formed due to gold atoms migration;
- hillocks have never been detected at SEM with a fast electromigration process, demonstrating that their formation derives from a phenomenon developing over time.

Sample 1a and 1b show two very different behaviors, even if they were part of the same wafer. However, as already mentioned at the beginning of this section, they did not underwent the same post-processing steps. Sample 1b was treated with one Oxygen ICP etch step lasting 1 min. Sample 1a instead underwent two steps of Oxygen ICP etch, each one having the same parameters of those used with 1b, for an aggregate time of 2 min. This post-processing step was used to ‘clean’ the surface of the devices, removing the organic contaminations that could influence the electrical properties of the tunnelling junctions. At the time of the choice of the post-processing steps, Oxygen ICP was expected to not affect the properties of the gold layer. Further investigations were thus performed to understand to which extent the Oxygen ICP could affect the electromigration process. In sections 6.3 and 6.4 these investigations on the side effects of Oxygen plasma are addressed.

6.3 Second Oxygen ICP on 1b

To find the cause of the different behavior of the samples 1a and 1b, a second Oxygen plasma etching was performed on 1b. This additional 1-minute Oxygen ICP allowed sample 1b to reach a very similar post-processing treatment of sample 1a (aggregate time of 2 min in Oxygen ICP).

After this new post-processing step, a new set of measurements was performed.

Tab.6 reports the results obtained. In this investigation, a fixed voltage was chosen and applied for a certain time, generally >5 min. The voltage was then increased if the process of conductance decrease slowed down significantly. This increase was performed for a maximum of a couple of times. In the table, only the last voltage used is reported.

Device #	Voltage	G_{init}/G_0	Time	R_{tun}	Outcome
1	300 mV	74	8 s	/	✓
2	300 mV	82	5 min	/	X
3	300 mV	104	5 min	/	X
4	240 mV	134	4 min	/	X
5	220 mV	40	150 s	/	✓
6	200 mV	63	5 min	48 M Ω	✓
7	200 mV	123	6 min	/	✓
8	300 mV	100	6 min	/	X
9	240 mV	112	2 min	/	✓
10	200 mV	129	<3 s	/	✓
11	250 mV	38	6 min	/	X
12	220 mV	113	8 s	5 G Ω	✓
13	280 mV	133	7 s	/	✓
14	200 mV	100	2 min	/	✓

Table 6: Summary of the electromigration investigation in 14 devices in sample 1b after the second run of Oxygen ICP. Only the last voltage used for each device is reported. G_{init}/G_0 is the initial normalized conductance of the bridge. The column **Time** reports the interval for which the voltage was applied. When <3 s, nanogap formation happened before that the first data point could be collected. R_{tun} is the tunnelling resistance at low bias. Not all nanogaps were conducting enough to allow for a resistance fitting at low bias. **Outcome** indicates for which device a gap is created after the electromigration process.

The results highlight a greater resistance to electromigration and nanogap formation than before the second run of Oxygen ICP. On average, an higher voltage was needed to start the process. A voltage $V \leq 200$ mV was successful in nanogap creation only in 4/14 (29%) against the 50% success rate in sample 1b before the second Oxygen plasma step. Fast electromigration (<10 s) processes leading to a nanogap could also be observed in 4/14 devices, while previously the minimum time was 1 min. Moreover rarely a tunnelling current at low bias could be detected. These results suggest that the second Oxygen ICP post-processing had influenced the electromigration process. However, the difference with sample 1a, which underwent the same fabrication and post-processing steps, are still clear. Indeed conductance steps could be observed in this sample, especially when a relatively low voltage, $V \leq 220$ mV, was applied. In addition, while sample 1a showed mostly quick electromigration processes, <1 min, in this one 5/9 still created a nanogap in a process lasting ≥ 2 min. These discrepancies are still unexplained and further investigations are needed to understand their origin.

Another proof that Oxygen ICP induces a change in the gold atoms migration dynamics is observed in SEM pictures taken after electromigration, that show the presence of hillocks near the ligaments, when the electromigration process did not create a gap. It has to be noted that hillocks formed on the side of the junction where the positive voltage was applied, strengthening the hypothesis that these structures are created due to the electron wind force action on the gold atoms.

This test confirmed that contrary to what was believed, Oxygen ICP has a effect on the gold layer, which can influence significantly the electromigration process. Since electromigration interests the superficial gold layer [43], the surface structural and morphological properties are highly influential on the process. It has been already reported that Oxygen plasma can oxidize gold surface [49], [50]. The oxidation of the surface is accompanied by the formation of hillocks, with an height of $\sim 20\text{nm}$ [50]. The origin of these micro-structures has been explained as the result of the relaxation of the compressive stresses brought about by the change of volume (~ 3 -fold increase) of the region involved in the oxidation. The same mechanism has been observed in other metals, for example Palladium [51].

Hillocks formation can be explained as the preferential growth during electromigration of micro-structures formed after the oxidation of the gold surface. This investigation proves once more that electromigration is very sensitive to the conductive layer structure and surface morphology, which can drive the evolution of the gold atom migration.

Fig.25 (see next page) illustrates a process in which hillocks are formed. The device is the #4 in Tab.6, which belongs to column S2. The S2 design features a wider neck, forming on average a larger number of ligaments. After ~ 3 min at $V=200$ mV, the voltage is increased to 240 mV for ~ 4 min. In both cases, the conductance was decreasing steadily but slowly. Even with a relatively mild process, with a maximum voltage applied of 240 mV for a total aggregate time of ~ 7 min, 3 hillocks grew close to the ligaments.

6.4 Long Oxygen ICP tests on 1d

Sample 1d originally underwent a 5-minutes Oxygen ICP, which greatly modified the surface morphology. For this reason it was never used for other research purposes. In this project, it has been studied to check the effect of a long Oxygen ICP treatment. In particular, hillocks formation was the key feature under investigation. One die, towards the center of the whole wafer, was chosen. All the 30 S3 devices were analyzed. As in the previous samples, first a low voltage measurement, in this case 50 mV, was performed to check the initial conductance of each device. Then the electromigration process started, applying a higher voltage that could induce electromigration, in this case $V \geq 200$ mV. Only in 8/30 devices the process could be performed, since a large fraction of the bridges already showed a gap or broke down when the needles were positioned on the pads. Indeed a feature of sample 1d is a larger than usual contact resistance of $\sim 50 \Omega$, which brings a complicated procedure to minimize it. This issue can be related to the deterioration of the gold layer after the long Oxygen ICP, which does not allow a good electrical contact with

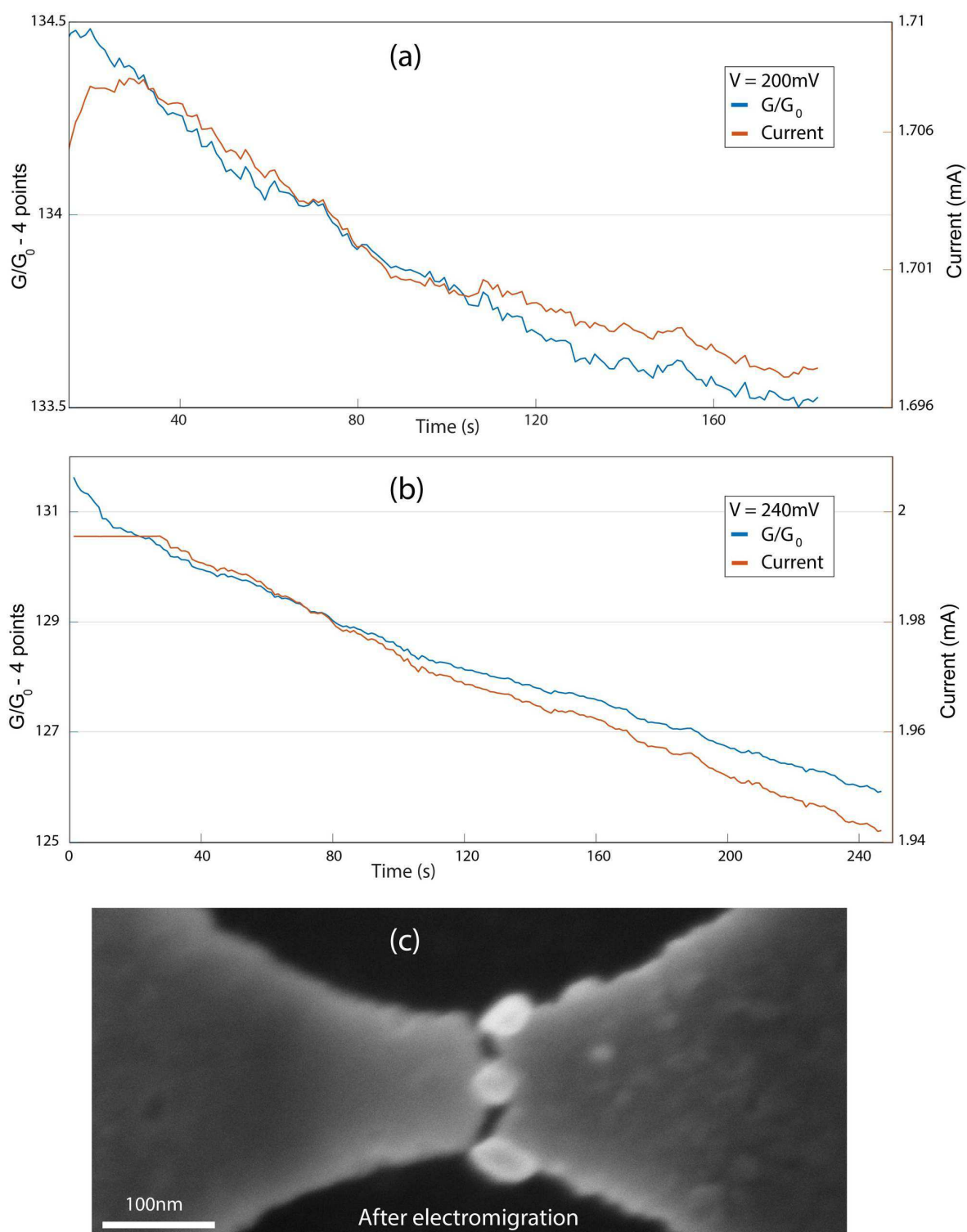


Figure 25: Illustration of an electromigration process in sample 1b after the second Oxygen ICP run. (a) First 200 mV are applied for ~ 3 min. Since the conductance was not decreasing substantially, the voltage was then increased (b) to 240 mV for ~ 4 min. (c) SEM picture after electromigration. 3 hillocks are clearly visible on the right of the ligaments, which is the positively biased side.

the needles. Tab.7 reports the results of the experiments performed on sample 1d.

Device #	Voltage	G_{init}/G_0	Time	R_{tun}	Outcome
1	220 mV	81	<3 s	/	✓
2	220 mV	102	10 min	67 MΩ	✓
3	220 mV	86	2 min	/	✓
4	220 mV	93	2 min	10 MΩ	✓
5	220 mV	99	16 min	/	X
	250 mV	11	80 s	/	✓
6	220 mV	93	2 min	2 GΩ	✓
7	200 mV	89	5 min	/	X
	230 mV	96	2 min	727 MΩ	✓
8	200 mV	88	4 min	/	X
	230 mV	94	80 s	28 MΩ	✓

Table 7: Summary of the electromigration investigation in 8 devices in sample 1d, which underwent a post-processing of 5 min in Oxygen ICP. G_{init}/G_0 is the initial normalized conductance of the bridge. The column **Time** reports the interval for which the voltage was applied. When <3 s, nanogap formation happened before that the first data point could be collected. R_{tun} is the tunnelling resistance at low bias. Not all nanogaps were conducting enough to allow for a resistance fitting at low bias. **Outcome** indicates for which device a gap is created after the electromigration process.

Surprisingly, 8/8 devices could create a gap with a relatively low voltage applied, $V \leq 250$ mV. Only 1 quick gap-forming electromigration (Time < 3 s) occurred, while the others show a large distribution of time. Moreover in 5/8 cases a tunnelling resistance in the linear region at low bias could be detected and extracted through a linear fitting. In this case a voltage sweep in a range from -100 mV to 100 mV was performed. Another feature of these devices is a almost constant conductance level in the first part of the process and then a sudden decrease, which most of the time led directly to the breakdown of the ligaments. This suggest that a fast and large displacement of atoms takes place at the onset of electromigration. In 2 devices however steps could be observed before breakdown. These results reveal that a 5 min exposure to Oxygen ICP does not accentuate the features induced with a 2 min exposure, but the whole process shows different modes of development.

SEM inspection showed surface with a large density of voids, which reach diameters of ~ 50 nm, considerably larger than the ones found in 1bb of ~ 20 nm. Accumulation of gold near the ligaments can be seen on the electrode with positive voltage applied, even if not as much pronounced as the ones seen in sample 1a. Moreover large regions of depleted gold are seen on the opposite side of junctions. This phenomenon is different from what was observed in sample 1a and 1b, where usually a reconfiguration of the ground-biased side, similar to melting took place. Further investigation is needed to understand the origin of these phenomena.

Fig.26 illustrates a typical electromigration breakdown in sample 1d, precisely in device #7 of Tab.7.

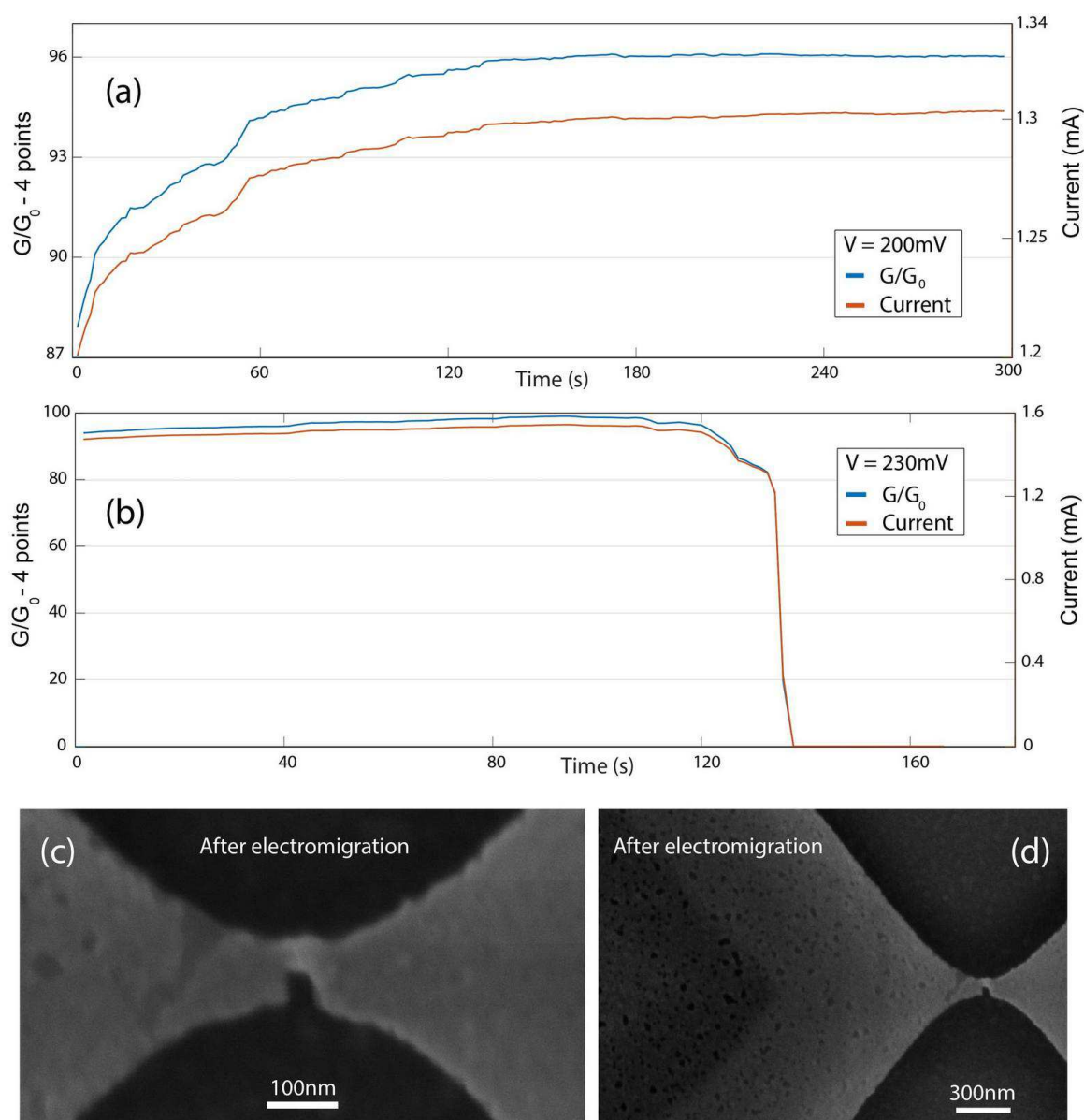


Figure 26: Illustration of an electromigration process in sample 1d, which underwent 5 min of Oxygen ICP run. (a) First 200 mV are applied for ~ 5 min. Since the conductance was not decreasing, the voltage was then increased (b) to 230 mV, inducing a nanogap formation after ~ 2 min. (c) SEM picture after electromigration, showing a little hillock grown in correspondence of the ligament. The nanogap is not clearly visible, even if $I(V)$ measurements demonstrate that a tunnelling transport mechanism is occurring. (d) The Au pad surface features a large density of voids after 5 min of Oxygen ICP. A larger void is visible close to the ligament after the electromigration, suggesting that atoms moved from the ground-biased side to the positively biased side of the bridge.

In the first part of the process, a voltage equal to 200 mV is applied for ~ 5 min. The conductance increases at first and then stabilizes. This feature was also observed in device #8 and few times also in the other samples. Rearrangement of the bridge due to electromigration is expected to be the reason of the conductance increase. In the second part of the process, the voltage is raised to 230 mV. Also in this case the conductance initially increase gradually. Then the conductance steps down a couple of times, before abruptly decreasing way below the conductance quantum. No steps are observed due to the ultra-fast process. SEM pictures do not show a clear gap between the two electrodes. However the current levels after the process are only compatible with tunnelling current. A small hillock can be seen in correspondence of the ligament, while a large void is on the left-side of the bridge. These pictures suggest that gold atoms have moved from the ground-biased side towards the Au bridge.

Fig.27 shows the effects of different exposures to Oxygen ICP. Larger voids and a larger density of them are observed increasing the process time. In sample 1d, where a 5 min exposure to Oxygen ICP was performed, voids have diameters of ~ 50 nm, while in sample 1c, which did not underwent any post-processing step, voids diameters are close to the resolution limit of SEM, reaching maximum values of ~ 15 nm.

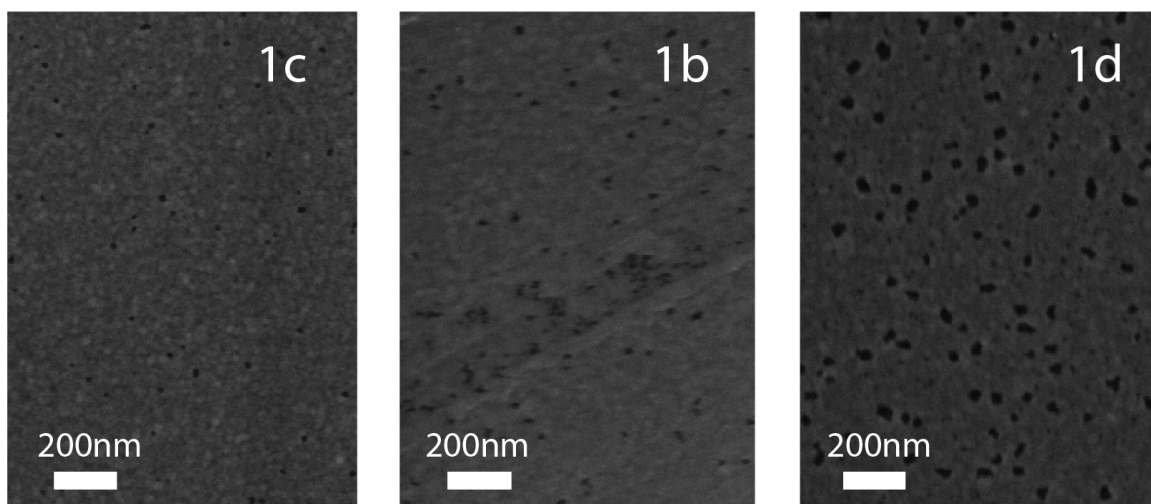


Figure 27: SEM pictures of the gold pads 3 of different samples. 1c did not undergo any Oxygen ICP, while 1b 2 min and 1d 5 min. The Oxygen plasma treatment, besides cleaning the surface from organic contaminations, affects the gold surface as well, inducing larger voids. These structural and morphological changes of the surface are responsible for a different electromigration process.

6.5 SEM influence on 1c



Figure 28: Sample 1c with the numeration of the dies used.

The concluding measurements were performed on sample 1c, which never underwent Oxygen ICP. Two dies were available in this quarter, both towards the center of the wafer. First measurements were carried out on die #1, in 21 devices in column S2. Tab.8 summarizes the results. The procedure consisted in applying first a very low voltage, in this case $V=50$ mV, to check the presence of Au ligaments connecting the two pads. When this was the case, the voltage was raised, enabling the beginning of electromigration. The voltage could be raised again when the process did not lead to a fast enough decrease of conductance. 13/21 devices had a conductive Au path between the two pads and could be used for this first investigation. Overall this first investigation led to good results, with low voltage needed to start the process and clearly visible steps before breaking. In 8/13 devices a relatively low voltage, i.e. $V \leq 220$ mV, could form a gap due to electromigration breakdown. Out of 10 devices which formed a gap, 6 showed evidence of tunnelling current in a low voltage sweep, between -100 mV and 100 mV. The linear fit of the tunnelling current led to low tunnelling resistance values, distributed in a range from 21 M Ω to 8 G Ω . Conductance steps could be detected, especially at low conductance values, i.e. $G < 10 \cdot G_0$ and with a low voltage applied, i.e. $V=200$ mV. Only in 3/10 a quick process, lasting less than 10 s, occurred. Overall the electromigration process resembled the one in sample 1b.

SEM inspection after electromigration showed no presence of hillocks for all the devices. Only in device #9, which underwent a long process with a voltage reaching the highest value of 280 mV, a structural reorganization could be observed on both sides of the bridge, close to the ligaments. In particular, SEM pictures show a smoother, grains-free Au surface close to the crack-line region. All the other devices do not present any feature induced by electromigration (Fig.29).

Device #	Voltage	G_{init}/G_0	Time	R_{tun}	Outcome
1	230 mV	58	4 s	/	✓
2	230 mV	80	4 min	21 M Ω	✓
3	230 mV	58	12 min	/	X
4	230 mV	45	2 min	68 M Ω	✓
5	220 mV	106	5 min	/	X
	250 mV	38	4 min	/	X
	300 mV	51	8 s	8 G Ω	✓
6	220 mV	85	70 s	226 M Ω	✓
7	220 mV	118	90 s	/	✓
8	200 mV	62	10 min	/	X
9	200 mV	129	3 min	/	X
	240 mV	129	6 min	/	X
	280 mV	95	4 min	/	X
10	200 mV	117	5 min	/	✓
11	200 mV	107	20 s	44 M Ω	✓
12	200 mV	70	8 min	/	X
	220 mV	4	5 min	/	X
	250 mV	3	50 s	111 M Ω	✓
13	200 mV	68	15 min	/	X
	220 mV	0.2	<3 s	/	✓

Table 8: Summary of the electromigration investigation in 13 devices in sample 1c, column S2, which did not undergo any post-processing in Oxygen ICP. G_{init}/G_0 is the initial normalized conductance of the bridge. The column **Time** reports the interval for which the voltage was applied. When <3 s, nanogap formation happened before that the first data point could be collected. R_{tun} is the tunnelling resistance at low bias. Not all nanogaps were conducting enough to allow for a resistance fitting at low bias. **Outcome** indicates for which device a gap is created after the electromigration process.

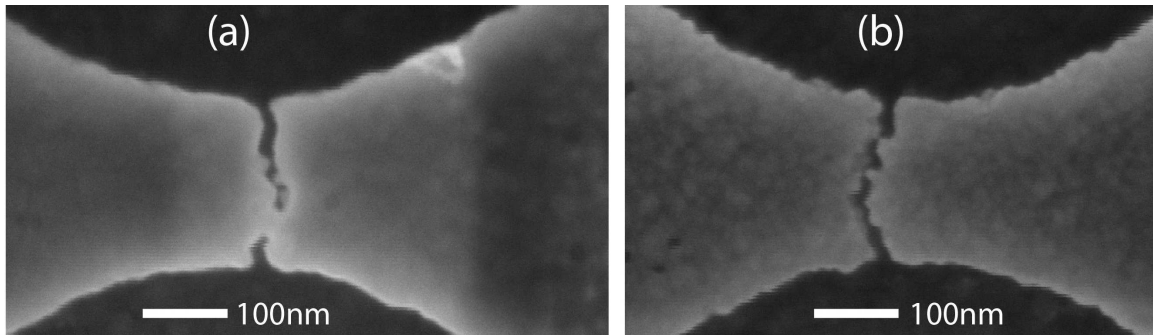


Figure 29: (a) SEM picture of device #9, where the electromigration process did not lead to a nanogap. Structural reorganization of the gold surface can be observed in the regions around the ligament. The surface in this area looks smoother and the Au grains are visible only in the external part of the image. (b) SEM picture of device #12. Nanogaps are formed after the electromigration process. Au grains are clearly visible all over the surface.

Before continuing the measurements on column S3 of the same die #1, a SEM inspection was performed to check the presence of resist close to the ligaments and to be able to compare the structure of the junction before and after the electromigration process. After the inspection 26/30 devices were selected. The remaining 4 were excluded, due to dust particles or crashed bridges by the needles after previous statistical analysis of initial resistance. The procedure in this case consisted in applying a fixed voltage of 230 mV, after the first measurement at 50 mV to check the initial conductance. The value $V=230$ mV was chosen based on the results displayed in Tab.8, being considered to lead to a good trade-off between yield of gap formation and tunnelling current level after breakdown. 15/26 devices could undergo the electromigration procedure, having $G_{init}/G_0 > 1$. Tab.9 and Tab.10 report the results of this investigation.

Device #	Voltage	G_{init}/G_0	Time	R_{tun}	Outcome
1	230 mV	88	<3 s	1 T Ω	✓
2	230 mV	112	15 min	/	X
3	230 mV	56	<3 s	11 G Ω	✓
4	230 mV	44	<3 s	2 T Ω	✓
5	230 mV	127	15 min	/	X
6	230 mV	100	8 s	/	✓
7	230 mV	83	7 s	117 G Ω	✓
8	230 mV	133	10 min	/	X
9	230 mV	97	10 min	/	X
10	230 mV	94	<3 s	973 G Ω	✓
11	230 mV	103	4 s	1 T Ω	✓
12	230 mV	30	<3 s	2 T Ω	✓
13	230 mV	98	10 min	/	X
14	230 mV	88	9 s	503 G Ω	✓
15	230 mV	96	<3 s	20 G Ω	✓

Table 9: Summary of the electromigration investigation in 15 devices in sample 1c, column S3, which did not undergo any post-processing in Oxygen ICP. G_{init}/G_0 is the initial normalized conductance of the bridge. The column **Time** reports the interval for which the voltage was applied. When <3 s, nanogap formation happened before that the first data point could be collected. R_{tun} is the tunnelling resistance at low bias. Not all nanogaps were conducting enough to allow for a resistance fitting at low bias. **Outcome** indicates for which device a gap is created after the electromigration process.

Sample-Die-Column	1c-1-S3
Gap originally present	11/26 (42%)
Gap not formed	5/26 (19%)
Gap formed	10/26 (39%)

Table 10: Summary of the measurements on sample 1c, die #1, column S3.

A different behavior from the one in column S2 is observed here. After this investigation, the devices could be divided in two groups: the ones which did not form a gap and the ones which underwent an abrupt decrease of conductance, leading to a gap formation, always in the first 10 s. There is a correlation between initial conductance and outcome of the process. All the 5 devices which did not form a gap featured $G_{init}/G_0 \geq 97$. Among the devices in which a gap was created, a tunnelling current could be detected in 9/10 cases in a low voltage sweep between -100 mV and 100 mV. However the tunnelling resistance values extracted are much higher than the one found in column S2. Here R_{tunn} ranges from 11 G Ω to 2 T Ω .

Fig.30 illustrate 3 different electromigration processes that took place in this investigation. The first image (a) shows the only clear hillock growth observed in die #1. Structural reorganization is also visible on the left side, which is at ground potential. The surface appears smoother in this region and Au grains can not be observed. Joule heating due to high current densities could contribute to this phenomenon. (b) and (c) display the two typical processes when a gap is formed. In particular (b) is a fast process, in which the first data point, measured after ~ 2.5 s, is related already to a tunnelling current. The granular structure of the gold surface is preserved in this case. An Au region in correspondence of the TiN crack-line appears to have a nanometric gap. SEM resolution does not allow determining with certainty the presence of a gap and its size. However this picture is completely compatible with a nanogap < 3 nm. (c) is a 10 min process, in which the conductance eventually reaches a stable level. A slight structural reorganization is visible on the left side of the ligament. 2 out of 3 ligaments broke during the process, leaving only one conductive path between the two pads.

Since these big differences between the two columns were never observed in the other samples, they were attributed to the high-magnification SEM inspection which was performed before the electromigration process. The SEM inspection could create a reconfiguration of the gold surface or charge it, influencing the migration of the Au atoms. To check this theory further measurements were carried out on die #2 on 4 devices which underwent an high-magnification SEM session and 4 devices which did not. Also in this case, the former featured an abrupt decrease of the conductance in the first seconds of the process, while the latter 4 did not create a gap in 10 min. Even if these results represent a strong clue to think that SEM inspection influences the Au atoms migration, further tests on a larger scale are needed to prove it. In addition, an investigation should be carried out to determine whether the difference in the two designs of columns S2 and S3 are responsible for this effects.

Overall this investigation is another proof that the electromigration process is regulated by several parameters, which determine the process speed, the formation of micro-structures and the structural reorganization of the region close to the ligaments. Different processes can regulate these parameters, e.g. Oxygen plasma and high magnification SEM inspection.

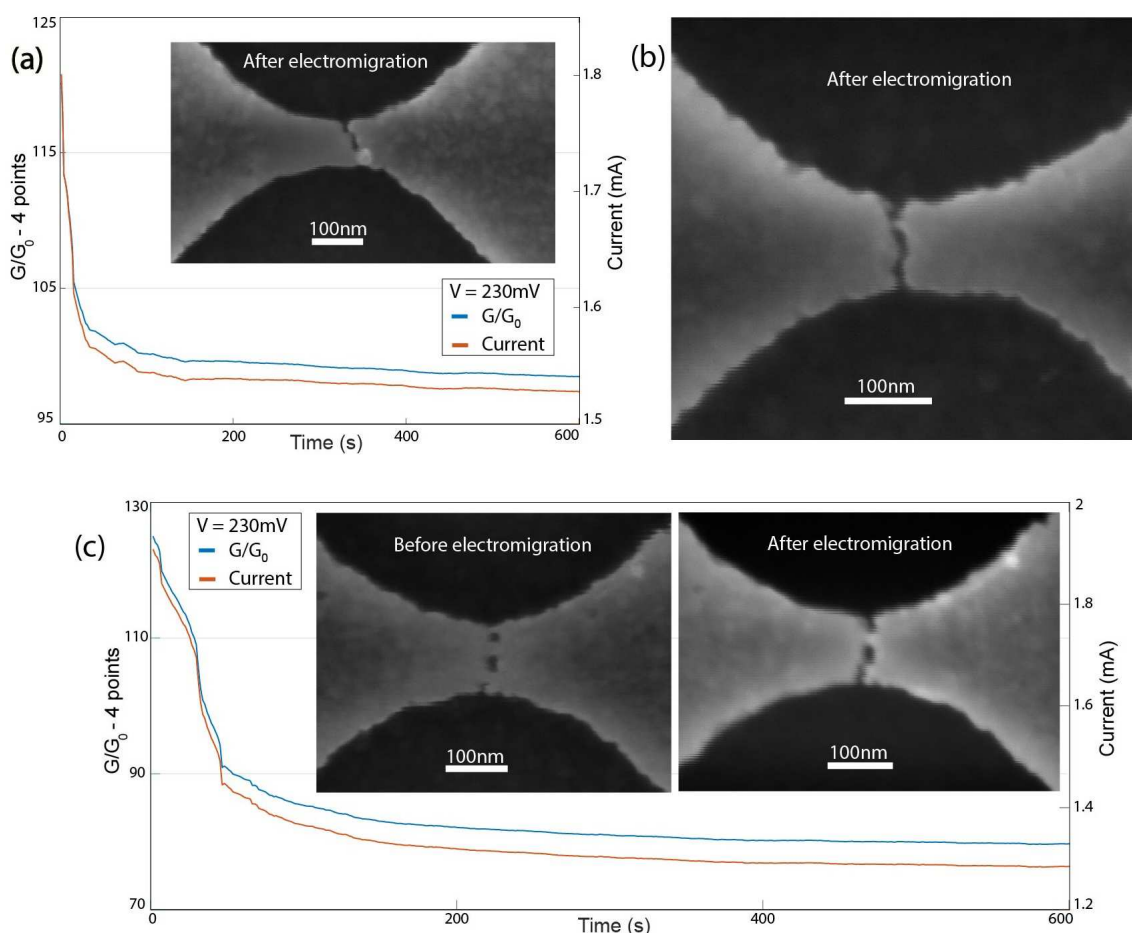


Figure 30: 3 examples of electromigration processes in sample 1c, die #1, column S3 after high magnification SEM inspection. (a) Device #5: process did not lead to a nanogap. An hillock close to the ligament and structural reorganization on the ground-biased side are clearly visible. (b) Device #1: fast process, a nanogap is formed. (c) Device #8: process did not lead to the breaking of all 3 ligaments. One ligament is still present, a slight structural reorganization has happened.

6.6 Final results on 1c

Final measurements were collected on die #2, avoiding SEM inspection before the measurements.

6.6.1 Statistical analysis of electromigration

51 devices were tested in columns S2 and S3. The protocol carried out on the devices consisted in applying first 50 mV to check the presence of ligaments bridging the two pads. When a conductance larger than $1 \cdot G_0$ was measured, the voltage was increased to 230 mV, for a maximum time of 10 minutes. 36/51 devices could be analyzed following this criteria, showing evidence of bridged pads. Measurements were stopped when due to electromigration $G < 0.01 \cdot G_0$. In the latter case, then a voltage ramp at low voltage was applied (0 V \rightarrow 0.1 V \rightarrow -0.1 V \rightarrow 0 V). Tab.11 and Tab.12 summarize the results.

Device #	Column	Voltage	G_{init}/G_0	Time	R_{tun}	Outcome
1	S2		gap			
2	S2	230 mV	90	<3 s	104 G Ω	✓
3	S2		gap			
4	S2	230 mV	65	<3 s	4 G Ω	✓
5	S2	230 mV	66	1 min	22 M Ω	✓
6	S2	230 mV	98	<3 s	80 G Ω	✓
7	S2	230 mV	20	10 min	/	X
8	S2	230 mV	94	<3 s	6 G Ω	✓
9	S2		gap			
10	S2	230 mV	66	10 min	/	X
11	S2	230 mV	81	10 min	/	X
12	S2	230 mV	137	10 min	/	X
13	S2	230 mV	65	5 min	159 M Ω	✓
14	S2	230 mV	65	<3 s	/	✓
15	S2		gap			
16	S2	230 mV	74	9 min	1 G Ω	✓
17	S2		gap			
18	S2		gap			
19	S2	230 mV	59	3 min	4 M Ω	✓
20	S2	230 mV	66	<3 s	240 G Ω	✓
21	S2		gap			
22	S2		gap			
23	S2		gap			
24	S2		gap			
25	S2	230 mV	33	30 s	42 G Ω	✓
26	S2	230 mV	95	10 min	/	X
27	S2	230 mV	36	45 s	284 M Ω	✓
28	S3		gap			
29	S3	230 mV	107	10 min	/	X
30	S3	230 mV	124	5 s	2 G Ω	✓
31	S3	230 mV	79	10 min	/	X
32	S3	230 mV	78	10 min	/	X
33	S3	230 mV	98	<3 s	/	✓
34	S3	230 mV	55	9 min	3 M Ω	✓
35	S3		gap			
36	S3	230 mV	51	<3 s	559 M Ω	✓
37	S3	230 mV	66	5 s	390 M Ω	✓
38	S3	230 mV	36	5 min	14 M Ω	✓
39	S3	230 mV	72	10 min	/	X
40	S3	230 mV	106	<3 s	95 G Ω	✓
41	S3	230 mV	58	3 min	322 M Ω	✓
42	S3		gap			

Continued on next page

43	S3		gap			
44	S3	230 mV	102	<3 s	216 GΩ	✓
45	S3	230 mV	87	10 min	/	X
46	S3	230 mV	99	10 min	/	X
47	S3	230 mV	70	10 min	/	X
48	S3	230 mV	102	10 min	/	X
49	S3	230 mV	71	10 min	/	X
50	S3	230 mV	9	10 min	/	X
51	S3		gap			

Table 11: Summary of the electromigration investigation in 51 devices in sample 1c, die #2, column S2 and S3, which did not undergo any post-processing in Oxygen ICP. G_{init}/G_0 is the initial normalized conductance of the bridge. ‘gap’ indicates that the initial conductance was below $1 \cdot G_0$, revealing the presence of a gap between the two electrodes. The column **Time** reports the interval for which the voltage was applied. When <3 s, nanogap formation happened before that the first data point could be collected. R_{tun} is the tunnelling resistance at low bias. Not all nanogaps were conducting enough to allow a resistance fitting at low bias. **Outcome** indicates for which device a gap is created after the electromigration process.

Sample-Die	1c-2
Gap originally present	15/51 (29.5%)
Connected - gap not created	15/51 (29.5%)
Connected - gap created	21/51 (41%)

Table 12: Summary of the measurements on sample 1c, die #2.

Among the total 51 devices taken into consideration, 36 underwent the electromigration process, having $G_{init}/G_0 > 1$. This fraction, corresponding to 71%, is in agreement with the statistical results introduced in section 6.2, although being below the average of the most central dies, corresponding to ~80% (sample 1a). It has to be noted that the designs present on this wafer have been chosen to study the formation of nanogaps immediately after the release of the TiN-Au bridges, with the CDBJ technology. Thus this percentage could be easily increased with a dedicated design, which would create on average a narrower gap in the titanium nitride, leading to a larger fraction of devices with ligaments connecting the two sides of the Au layer. A possible decrease of the yield of nanogap formation through electromigration could arise though. Further experimental effort is needed to find the optimal design of the bridges.

21/36 (58%) devices formed a gap due to the electromigration process. Also in this case this data is not far from correspondent results in the other samples. Among the 21 that were connected before electromigration and then formed a gap, 10 showed a conductance $G < 0.01 \cdot G_0$ at the first data point, usually after 2.5 seconds, and 11 showed a distribution of time from 5 seconds to 9 minutes, as reported in Fig.31.

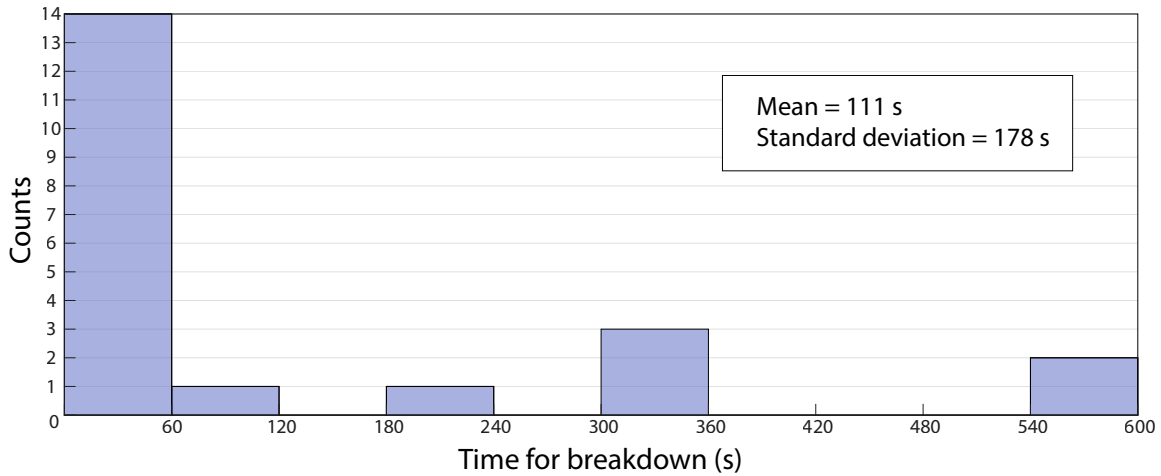


Figure 31: Histogram illustrating the distribution of time needed to create a gap through electromigration in the 21 devices analyzed. 10 bins of 60 s each are used.

Conductance steps before the breakdown are visible in most of the devices which did not undergo a fast electromigration process. After breaking, 19/21 devices could generate a detectable tunnelling current at low bias, between -0.1 V and 0.1 V. In this range the $I(V)$ curve is linear and a linear fitting can be performed. The extracted values of resistance are reported in Tab.11. In general R_{tun} is relatively low compared to the ones extracted in the other samples, ranging from 4 M Ω to 240 G Ω . These values are only compatible with tunnelling currents through nanogaps whose width is <3 nm. When the electromigration process did not successfully lead to a gap, usually at first a clear reduction of conductance was observed, then the rate of change decreased over time, reaching eventually a stable level of conductance.

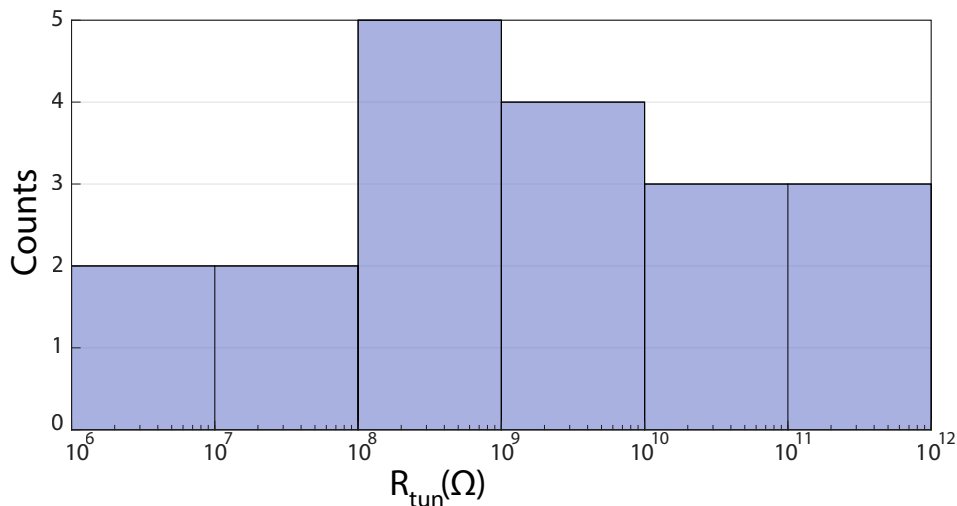


Figure 32: Histogram illustrating the distribution of tunnelling resistance values fitted from the $I(V)$ curves in the linear region after gap formation. 19 devices are analyzed. A logarithmic scale is used for R_{tun} and 6 bins are extracted, each one spanning over one order of magnitude, from 1 M Ω to 1 T Ω .

The yield of the process seems to be weakly correlated to the initial conductance of the bridge when the latter is large. Indeed when $G_{init}/G_0 > 80$ the distribution of initial conductance in the devices forming a gap and devices not forming a gap at the end of the process, is basically the same. However when $G_{init}/G_0 < 70$, in 13/16 (81%) devices the electromigration successfully led to a gap. On the other hand only 8/20 (40%) form a gap when $G_{init}/G_0 \geq 70$. Thus the nanogap formation is eased when the initial conductance is in the low values range, that is to say when the resistance is dominated by the contribution of the ligaments.

SEM inspection after the measurements showed no large hillocks, but in some cases a feeble accumulation of material on the positively biased electrode. On the 0V-biased electrode, when the voltage was applied for the whole 10 minutes without successful gap formation, few times structural reorganization could be observed. In the latter case, in correspondence of the TiN crack, Au grains are not visible and the surface looks smoother.

6.6.2 Typical electromigration processes

Fig.33 illustrates 3 different typical electromigration processes observed within the 36 devices investigated in die #2 of sample 1c.

In the first image (a), device #38, the procedure leads to the formation of a nanogap after a 5 min process. Thus several data points are collected before observing a conductance way below $1 \cdot G_0$. The latter condition took place in 11/36 devices, with a time distribution of formation of the gap between 5 s and 9 min. Discrete levels of conductance are clearly visible at $2 \cdot G_0$ and $1 \cdot G_0$. At the moment of breakdown, the conductance drops from $\sim 0.7 \cdot G_0$ to below $0.01 \cdot G_0$, revealing the transition of transport mechanism from ballistic to tunnelling regime. A common feature of the devices in this sample is the decrease of conductance measured at the first data point with respect to the 50 mV measurement. In this case, the first point collected with 230 mV is at $\sim 9 \cdot G_0$, while when 50 mV were applied, the conductance was stable at $36 \cdot G_0$. The I(V) curve at low voltage highlights a linear trend, as expected from the theory. The fitted value of tunnelling resistance is 14 M Ω . The SEM image after the process is compatible with the presence of a single nanogap. SEM resolution of ~ 5 nm does not allow measuring the gap width.

In image (b), corresponding to device #2, the conductance is well below the conductance quantum, namely at $\sim 10^{-6} \cdot G_0$, at the first data point, collected after ~ 2.5 s. This scenario was observed in 10/36 devices. The I(V) fit returns a value of tunnelling resistance of 104 G Ω . The SEM image displays two nanogaps. It has to be noted that this device belonged to column S2, which has a wider constriction than S3, leading to a larger average number of ligaments.

15/36 devices did not form a gap after the 10 min process, as in case (c), corresponding to device #29. Generally at first the conductance decreases with a good rate, then the process slows down and eventually the conductance reaches a stable level. The SEM picture shows a ligament connecting the two sides of the bridge. Some structural reorganization is distinguishable around the region of the ligament. On the left side, the surface looks smoother and the Au grains are not visible. On the right side of the ligament there is instead a brighter grain, suggesting the growth of an hillock during electromigration.

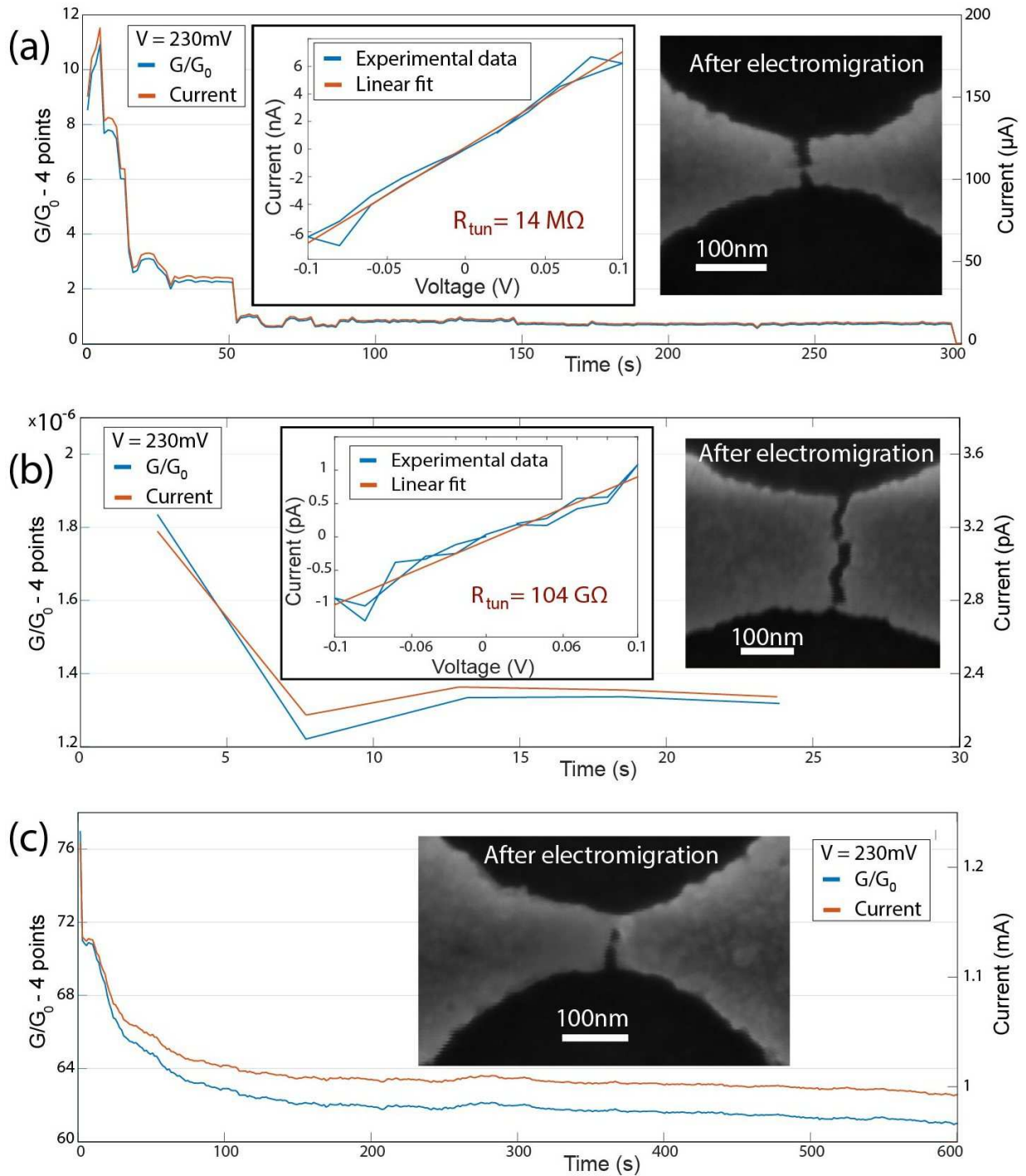


Figure 33: (a) Device #38: 5 min process, in which conductance steps are observed. The insets show the I(V) curve, with its linear fit, and a SEM image after the process. (b) Device #2: quick electromigration process. The conductance is well below $1 \cdot G_0$ at the first data point. The inset on the left shows the I(V) curve, with its linear fit. In the right side inset is displayed a SEM image after the process, where two nanogaps are visible. SEM pictures do not allow determining whether the tunnelling current is dominated by one of the two gaps. (c) Device #29: gap not formed. The rate of reduction of conductance decreases over time and after 10 min $G = 61 \cdot G_0$. The SEM image in the inset displays a small hillock on the right side of the ligament and a structurally reorganized region on the left side.

6.6.3 Final considerations on 1c, die #2

Sample 1c showed a good electromigration process behavior, similar to that observed in sample 1b. However overall the results obtained in sample 1b, in terms of yield, voltage required and reproducibility, are still unmatched. Here it is reported a list of features and statistical results obtained in this sample, in particular in the 51 devices analyzed in die #2:

- relatively low breakdown voltage, with 21/36 (58%) devices creating a nanogap from ligament(s) with a breakdown voltage $V = 230$ mV;
- tunnelling current after nanogap formation measurable in 19/21 the devices, using low voltage sweeps, between -0.1 V and 0.1 V. This fraction could be increased with wider range voltage sweeps;
- tunnelling resistance at low bias between 4 M Ω to 240 G Ω ;
- considerably larger yield when the starting conductance is low. In particular when $G_{init}/G_0 < 70$, 13/16 (81%) formed a gap;
- considering not usable the devices which already presented a gap before the electromigration process, the overall yield of gap formation is 21/51 (41%);
- considering only the devices which showed a measured tunnelling current at low voltage, the overall yield is 19/51 (37%);
- considering the devices which formed a gap, a gradual decrease of the conductance, with steps clearly visible before the breakdown was observed in 11/21 devices;
- considering the devices which formed a gap, a very fast process (< 3 s) was observed in the remaining 10/11 devices;
- few hillocks formed, limited to some processes which did not lead to a nanogap and lasting for a long time, namely 10 min;
- structural reorganization on the 0V-biased side when the process lasted 10 min in most of the cases.

7 Conclusions

A new methodology to fabricate tunnelling nanogap junctions has been developed. The methodology consists in the electromigration of nanometer-sized ligaments formed with the process of fabrication of crack-defined break-junctions (CDBJs). Due to the nanometric size of the ligaments, a feedback-free electromigration process is made possible. In this process, an optimal fixed voltage is applied for a limited time. Another advantage of this methodology resides in having suspended ligaments, avoiding the common problem of debris created during electromigration in the vicinity of the gap. The first sample analyzed (sample 1b) showed optimal features of electromigration. In particular it featured gradual decrease of the conductance over time, observation of conductance steps before the breakdown, relatively low voltage needed to create a gap ($V \leq 200$ mV in 9/18 cases), detectable tunnelling current after breakdown and good yield, with all the devices being able to form a gap providing that the voltage assumed values as high as 1 V. Following measurements in other samples highlighted the very sensitive nature of the electromigration process, which can be heavily influenced by Oxygen ICP post-processing and high-magnification SEM inspection. Final measurements (sample 1c) led to a total yield of 37% of fabrication of tunnelling nanogap junctions, choosing an optimal voltage of 230 mV. However this is a conservative number since all the devices which already showed a gap (15/51) with the CDBJs methodology are excluded from the count of working devices. Moreover the bridges analyzed in this work were not designed for the scope of electromigration-induced formation of nanogaps and several factors, as post-processing steps and grain structure of the metal layer, could be tuned and optimized. A 2-fold improvement of the total yield can be estimated based on the results obtained with sample 1b and on the aforementioned considerations. Nevertheless the 37% yield obtained with the last sample is still a large improvement with respect to the CDBJs methodology (7%). It has to be noted that this additional electromigration step in the fabrication transforms a wafer-scale parallel process in a serial process. However being a simple step, which does not require any feedback control, as it is commonly the case for electromigrated break-junctions, a possible development could include the parallelization of the process to several devices. Since the fabrication methodology of CDBJs is compatible with CMOS technology, these devices can be integrated on top of CMOS circuits. In this scenario the problem of parallel electromigration and then single addressability of each device can be solved with conventional solid-state integrated electronic circuits (ICs).

Overall this Thesis introduces a new methodology to create tunnelling nanogaps junctions for fundamental research applications, as molecular transport study and biomolecular detection, and represents a first step in the realization of large arrays of Au tunnelling nanogap junctions, with a total yield way larger than the one of CDBJs, which is, at the moment of the writing of this Thesis, the only wafer-scale process for the realization of metallic tunnelling nanogap junctions reported in literature.

References

- [1] Massimiliano Di Ventra and Masateru Taniguchi. “Decoding DNA, RNA and peptides with quantum tunnelling”. In: **Nature nanotechnology** 11.2 (2016), p. 117.
- [2] Riccardo Frisenda et al. “Electrical properties and mechanical stability of anchoring groups for single-molecule electronics”. In: **Beilstein journal of nanotechnology** 6 (2015), p. 1558.
- [3] Qiang Zhao et al. “Nanoscale electrodes for flexible electronics by swelling controlled cracking”. In: **Advanced Materials** 28.30 (2016), pp. 6337–6344.
- [4] Daniel R Ward et al. “Optical rectification and field enhancement in a plasmonic nanogap”. In: **Nature nanotechnology** 5.10 (2010), p. 732.
- [5] Valentin Dubois et al. “Massively parallel fabrication of gold break junctions featuring sub-3 nm gaps for molecular devices”. In: **Nature communications** (2018).
- [6] Gordon E Moore. “Cramming more components onto integrated circuits, Reprinted from Electronics, volume 38, number 8, April 19, 1965, pp. 114 ff.” In: **IEEE Solid-State Circuits Society Newsletter** 11.3 (2006), pp. 33–35.
- [7] International Technology Roadmap for Semiconductors 2013 edition. Accessed August 7 2018. URL: www.semiconductors.org/clientuploads/Research_Technology/ITRS/2013/2013PIDS.pdf.
- [8] R Lloyd Carroll and Christopher B Gorman. “The genesis of molecular electronics”. In: **Angewandte Chemie International Edition** 41.23 (2002), pp. 4378–4400.
- [9] Andrew Steane. “Quantum computing”. In: **Reports on Progress in Physics** 61.2 (1998), p. 117.
- [10] Kevin Davies. **The \$ 1000 genome: the revolution in DNA sequencing and the new era of personalized medicine**. Simon and Schuster, 2015.
- [11] Frederick Sanger, Steven Nicklen, and Alan R Coulson. “DNA sequencing with chain-terminating inhibitors”. In: **Proceedings of the national academy of sciences** 74.12 (1977), pp. 5463–5467.
- [12] K. Wetterstrand. ”DNA sequencing costs: Data from the nhgri genome sequencing program (gsp)” Accessed August 7 2018. URL: www.genome.gov/sequencingcostsdata/.
- [13] Grégory F Schneider and Cees Dekker. “DNA sequencing with nanopores”. In: **Nature biotechnology** 30.4 (2012), p. 326.
- [14] Cees Dekker. “Solid-state nanopores”. In: **Nature nanotechnology** 2.4 (2007), p. 209.
- [15] Ch Joachim et al. “Electronics using hybrid-molecular and mono-molecular devices”. In: **Nature** 408.6812 (2000), p. 541.

-
- [16] Xing Chen et al. “Electrical nanogap devices for biosensing”. In: **Materials Today** 13.11 (2010), pp. 28–41.
- [17] Shuming Nie and Steven R Emory. “Probing single molecules and single nanoparticles by surface-enhanced Raman scattering”. In: **science** 275.5303 (1997), pp. 1102–1106.
- [18] Johannes Kern et al. “Electrically driven optical antennas”. In: **Nature Photonics** 9.9 (2015), p. 582.
- [19] URL: www.int.kit.edu/wenzel.php.
- [20] Siwapon Srisonphan, Yun Suk Jung, and Hong Koo Kim. “Metal–oxide–semiconductor field-effect transistor with a vacuum channel”. In: **Nature nanotechnology** 7.8 (2012), p. 504.
- [21] Jeong Oen Lee et al. “A sub-1-volt nanoelectromechanical switching device”. In: **Nature nanotechnology** 8.1 (2013), p. 36.
- [22] Songmei Wu et al. “Molecular junctions based on aromatic coupling”. In: **Nature nanotechnology** 3.9 (2008), p. 569.
- [23] Takahito Ohshiro et al. “Single-molecule electrical random resequencing of DNA and RNA”. In: **Scientific reports** 2 (2012), p. 501.
- [24] Zheng Ming Wu et al. “Feedback controlled electromigration in four-terminal nanojunctions”. In: **Applied Physics Letters** 91.5 (2007), p. 053118.
- [25] Dong Xiang et al. “Mechanically controllable break junctions for molecular electronics”. In: **Advanced Materials** 25.35 (2013), pp. 4845–4867.
- [26] K O’Neil, HSJ Van der Zant, and EA Osorio. “Self-breaking in planar few-atom Au constrictions for nm-spaced electrodes”. In: **Applied Physics Letters** (2007).
- [27] Jianchun Dong and Babak A Parviz. “Using noise for controlled disassembly of nanoscale gold wires”. In: **Nanotechnology** 17.20 (2006), p. 5124.
- [28] Daewon Ha et al. “Highly manufacturable 7nm FinFET technology featuring EUV lithography for low power and high performance applications”. In: **VLSI Technology, 2017 Symposium on**. IEEE. 2017, T68–T69.
- [29] Xinyu Zhao et al. “Minimization of line edge roughness and critical dimension error in electron-beam lithography”. In: **Journal of Vacuum Science & Technology B, Nanotechnology and Microelectronics: Materials, Processing, Measurement, and Phenomena** 32.6 (2014), 06F505.
- [30] Ampere A Tseng, Andrea Notargiacomo, and TP Chen. “Nanofabrication by scanning probe microscope lithography: A review”. In: **Journal of Vacuum Science & Technology B: Microelectronics and Nanometer Structures Processing, Measurement, and Phenomena** 23.3 (2005), pp. 877–894.
- [31] E Salvati et al. “Nanoscale structural damage due to focused ion beam milling of silicon with Ga ions”. In: **Materials Letters** 213 (2018), pp. 346–349.
- [32] GJ Dolan. “GJ Dolan, *Appl. Phys. Lett.* 31, 337 (1977).” In: **Appl. Phys. Lett.** 31 (1977), p. 337.

- [33] AF Morpurgo, CM Marcus, and DB Robinson. “Controlled fabrication of metallic electrodes with atomic separation”. In: **Applied Physics Letters** 74.14 (1999), pp. 2084–2086.
- [34] I Petrov et al. “Microstructural evolution during film growth”. In: **Journal of Vacuum Science & Technology A: Vacuum, Surfaces, and Films** 21.5 (2003), S117–S128.
- [35] Valentin Dubois, Frank Niklaus, and Göran Stemme. “Crack-Defined Electronic Nanogaps”. In: **Advanced Materials** 28.11 (2016), pp. 2178–2182.
- [36] Valentin Dubois, Frank Niklaus, and Göran Stemme. “Design and fabrication of crack-junctions”. In: **Microsystems & Nanoengineering** 3 (2017), p. 17042.
- [37] Jose I Gonzalez et al. “Quantum mechanical single-gold-nanocluster electroluminescent light source at room temperature”. In: **Physical review letters** 93.14 (2004), p. 147402.
- [38] Hubert B Heersche et al. “Kondo effect in the presence of magnetic impurities”. In: **Physical review letters** 96.1 (2006), p. 017205.
- [39] James R Black. “Electromigration failure modes in aluminum metallization for semiconductor devices”. In: **Proceedings of the IEEE** 57.9 (1969), pp. 1587–1594.
- [40] ML Trouwborst, SJ Van Der Molen, and BJ Van Wees. “The role of Joule heating in the formation of nanogaps by electromigration”. In: **Journal of Applied Physics** 99.11 (2006), p. 114316.
- [41] HV Nguyen et al. “Effect of thermal gradients on the electromigration lifetime in power electronics”. In: **Reliability Physics Symposium Proceedings, 2004. 42nd Annual. 2004 IEEE International**. IEEE. 2004, pp. 619–620.
- [42] A Mangin et al. “Reduced work functions in gold electromigrated nanogaps”. In: **Physical Review B** 80.23 (2009), p. 235432.
- [43] Douglas R Strachan et al. “Real-time TEM imaging of the formation of crystalline nanoscale gaps”. In: **Physical Review Letters** 100.5 (2008), p. 056805.
- [44] Janez Bonca and Sergei Kruchinin. **Electron transport in nanosystems**. Springer Science & Business Media, 2008.
- [45] John G Simmons. “Generalized formula for the electric tunnel effect between similar electrodes separated by a thin insulating film”. In: **Journal of applied physics** 34.6 (1963), pp. 1793–1803.
- [46] K Hansen et al. “Current-voltage curves of gold quantum point contacts revisited”. In: **Applied Physics Letters** 77.5 (2000), pp. 708–710.
- [47] Paul S Bagus et al. “Work function changes induced by charged adsorbates: Origin of the polarity asymmetry”. In: **Physical review letters** 100.12 (2008), p. 126101.

- [48] DR Strachan et al. “Controlled fabrication of nanogaps in ambient environment for molecular electronics”. In: **Applied Physics Letters** 86.4 (2005), p. 043109.
- [49] D Berman and J Krim. “Impact of oxygen and argon plasma exposure on the roughness of gold film surfaces”. In: **Thin Solid Films** 520.19 (2012), pp. 6201–6206.
- [50] B Koslowski et al. “Oxidation of preferentially (1 1 1)-oriented Au films in an oxygen plasma investigated by scanning tunneling microscopy and photoelectron spectroscopy”. In: **Surface science** 475.1-3 (2001), pp. 1–10.
- [51] S Aggarwal et al. “Spontaneous ordering of oxide nanostructures”. In: **Science** 287.5461 (2000), pp. 2235–2237.

8 Appendices

Appendix 1: schematic drawing of a die

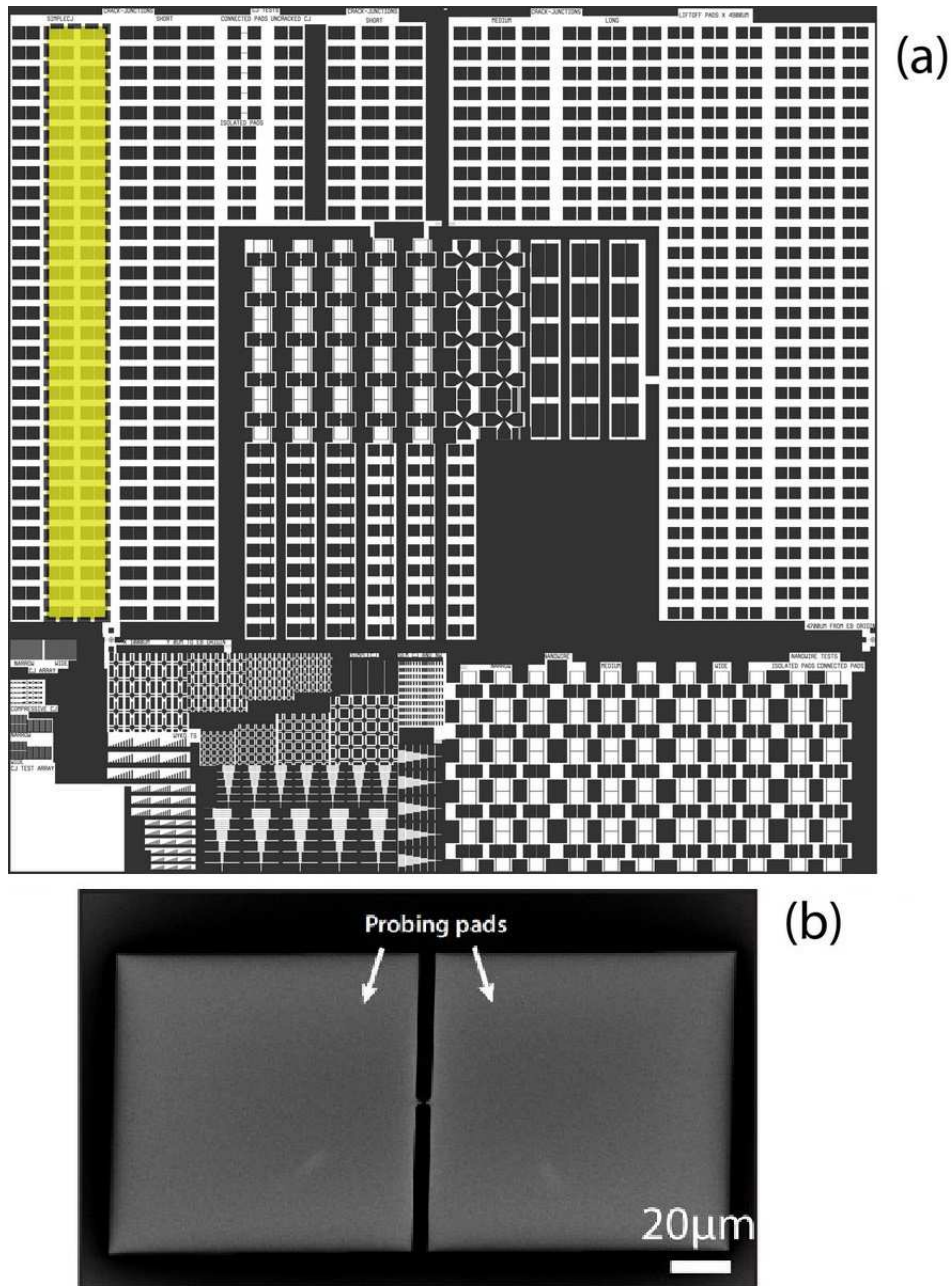


Figure 34: (a) Schematic top view drawing of a die. In yellow are highlighted the two column S2 and S3, respectively on the left and the right, containing the devices used in this Thesis. Each die occupies an area of $7 \times 7 \text{mm}^2$ on the wafer. (b) SEM image of a single device, including two $100 \mu\text{m} \times 100 \mu\text{m}$ sized probing pads connected to each electrode. Reproduced from [5].

Appendix 2: conversion from normalized conductance to resistance

G/G_0	$R(\Omega)$
1	12906
2	6453
3	4302
4	3227
5	2581
10	1291
20	645
30	430
40	323
50	258
60	215
70	184
80	161
90	143
100	129
110	117
120	108
130	99
140	92
150	86

Table 13: List of values of normalized conductance G/G_0 , with the correspondent value of resistance, to help the reader switch from one unit of measurement to the other. In general to convert quickly a normalized conductance to a resistance measured in Ω , the equation is $R(\Omega) = R_0 / (G/G_0) \approx 12.9 \cdot 10^3 \Omega / (G/G_0)$. The highest value of normalized conductance measured in a device under test in this Thesis has been $G/G_0 = 137$.

Appendix 3: tunnelling current fit

Parameters extraction from $I(V)$ tunnelling curve was performed on several devices discussed in this Thesis. A 1D transmission model with a single transmission channel was used, using Eq.18 as the fitting function, namely:

$$I(V) = \frac{2e}{h} \int_0^\infty [f(E) - f(E - eV)] \cdot T(E, V) dE$$

$T(E, V)$ is the transmission probability. According to the Wentzel Kramers Brillouin (WKB) approximation:

$$T(E, V) = \exp\left\{-\int_0^s \frac{4\pi}{h} \sqrt{2m[\phi(z, V) - E]} dz\right\}$$

The potential profile along the gap $\phi(z, V)$ is approximated as a tilted trapezoidal barrier:

$$\phi(z, V) = \phi_L + (\phi_R - \phi_L - eV) \cdot \frac{z}{d}$$

A non-linear least squares solver was used on MATLAB to perform the fitting. In the $I(V)$ function used, 3 parameters have to be extracted: d , ϕ_L and ϕ_R , respectively the gap width, the potential barrier on the left side and the potential barrier on the right side. The voltage is applied to the right side in this model. During the studies, it was found that a symmetric model ($\phi_L = \phi_R$) produced better results. Indeed asymmetric models returned in few cases very different values of ϕ_L and ϕ_R , with one of the two parameters corresponding to the lower or higher limit assumed in the MATLAB script, corresponding to 0.01 eV and 5 eV.

Appendix 4: parameters extraction in sample 1c, die #2

Device #	d (nm)	ϕ (eV)	R^2
2	1.075	2.10	0.93
4	1.956	0.43	0.98
5	0.349	4.32	0.97
6	1.057	2.09	0.93
8	0.681	3.74	0.92
13	2.202	0.22	0.96
16	0.559	4.10	0.90
19	0.255	5.00	0.99
20	1.108	2.17	0.72
25	1.001	2.14	0.81
27	1.700	0.36	0.94
30	1.603	0.64	0.87
34	1.605	0.15	0.97
36	0.686	2.32	0.95
37	0.470	5.00	0.87
38	0.324	4.50	0.99
40	1.069	2.10	0.83
41	1.541	0.43	0.99
44	1.103	2.15	0.39

Table 14: Table displaying the fitted parameters obtained from the I(V) tunnelling curve of the 19 devices in Tab.11 (die #2 of sample 1c) in which a tunnelling current could be detected. A symmetrical 1D transmission model was used for the fitting procedure, which is described in Appendix 3. **Device #** reports the number corresponding to the same device in Tab.11. **d (nm)** is the fitted gap width. ϕ is the potential barrier height ($\phi = \phi_L = \phi_R$). R^2 corresponds to the coefficient of determination.